Ann. Phys. (Berlin) **527**, No. 1–2, 45–80 (2015) / DOI 10.1002/andp.201400160

annalen der physik

Review Article

# Classical and fluctuation-induced electromagnetic interactions in micron-scale systems: designer bonding, antibonding, and Casimir forces

*Alejandro W. Rodriguez*[1,*], *Pui-Chuen Hui*[2], *David P. Woolf*[2], *Steven G. Johnson*[3], *Marko Lončar*[2], *and Federico Capasso*[2]

Received 29 July 2014, revised 10 September 2014, accepted 11 September 2014

Whether intentionally introduced to exert control over particles and macroscopic objects, such as for trapping or cooling, or whether arising from the quantum and thermal fluctuations of charges in otherwise neutral bodies, leading to unwanted stiction between nearby mechanical parts, electromagnetic interactions play a fundamental role in many naturally occurring processes and technologies. In this review, we survey recent progress in the understanding and experimental observation of optomechanical and quantum-fluctuation forces. Although both of these effects arise from exchange of electromagnetic momentum, their dramatically different origins, involving either real or virtual photons, lead to different physical manifestations and design principles. Specifically, we describe recent predictions and measurements of attractive and repulsive optomechanical forces, based on the bonding and antibonding interactions of evanescent waves, as well as predictions of modified and even repulsive Casimir forces between nanostructured bodies. Finally, we discuss the potential impact and interplay of these forces in emerging experimental regimes of micromechanical devices.

## 1 Introduction

Light can exert a force. Although this statement is uncontroversial today, its confirmation was a remarkable triumph a little over a century ago [1], only a couple of centuries after scientists had finally managed to show that light moves at all (as opposed to appearing instantaneously). Much of the early treatment of this force was limited to light incident on planar surfaces described by some absorption and reflection coefficients, in which the resulting "radiation pressure" can be explained by intuitive arguments that continue to dominate pedagogical materials. Perversely, this classical force is easiest to understand through a quantum picture [2]: since a photon with energy $U$ has relativistic momentum $U/c$, a black surface that completely absorbs normal-incident light with power $P$ should experience a force $P/c$, corresponding to the rate at which it receives momentum. Similar arguments apparently imply, from conservation of momentum, that light can only "push" on a flat surface (with a force of at most $2P/c$) and can never "pull."

However, in microstructured systems, the forces induced by electromagnetic waves are complicated by a number of additional possibilities. One can consider forces induced by guided waves, resonant modes, and evanescent waves in addition to forces exerted by incident waves from vacuum, which can both change the nature of the force and (thanks to spatiotemporal localization) greatly enhance its strength. In systems with multiple components, one component can either pull or push a neighboring component, since momentum-conservation restrictions only apply to the net force on all components rather than to the force on any individual object. Even for an isolated object, focused beams on a small object can scatter oblique light forward, a transfer of momentum from the object to the wave that creates an optical "tractor beam" [3]. We review many of these possibilities and their applications in Section 2.

In addition to these geometric and localization effects, Section 3 reviews another consideration that arises for optical forces at submicron scales: classical

---

[*] Corresponding author E-mail: arod@princeton.edu

[1] Department of Electrical Engineering, Princeton University, Princeton, NJ, USA

[2] School of Engineering and Applied Sciences, Harvard University, Cambridge, MA, USA

[3] Department of Mathematics, Massachusetts Institute of Technology, Cambridge, MA, USA

optical forces arise from external sources of electromagnetic fields, but there are also *internal* sources, namely thermal and quantum charge oscillations. Most famously, the vibrations of matter give rise to thermal radiation, the familiar glow of hot objects [4], but the same fields carry momentum as well as energy. Intuitively, two hot objects will push each other apart with their thermal radiation, but this picture is incomplete because it does not include ambient radiation, and the effect is dramatically altered for objects in thermal equilibrium with their environment. For well-separated objects in thermal equilibrium, the omnidirectional radiation from both the objects and their environment exactly cancels and there is no net force on any object, but for surfaces at submicron separations the evanescent coupling and other effects tend to produce an *attractive* force. In the limit of zero temperature, this attractive force remains due to quantum fluctuations and is known as a “Casimir” force [5]. For a single pair of atoms, the same phenomenon is a van der Waals force known as the “London-dispersion” force (or the “Casimir–Polder” force once wave effects are included) [6]. (Although such forces have a sometimes bewildering variety of theoretical descriptions, ranging from zero-point energy sums to path-integral models, it turns out that all of these expressions are mathematically equivalent to the forces of fields produced by vibrating charges in matter [194].) Casimir forces between parallel metallic surfaces, first predicted in 1948 and reviewed in Section 3.2.2, were finally observed quantitatively in 1978 [8] and have subsequently been measured in a wide variety of microelectromechanical systems (MEMS) with increasing precision [9]. However, until the last decade, both theoretical predictions and experiments were limited to planar or near-planar geometries with the exception of a handful of theoretical special cases. This has now changed, thanks to both powerful new computational tools and rapidly expanding capabilities of micromechanical experiments, enabling an explosion in *designer* Casimir forces (reviewed in Section 3.2) with exotic properties extending far beyond simple attraction between parallel surfaces. Because Casimir forces remain when all other electromagnetic interactions (external fields, static charges, and so on) are removed, Section 3.3 explains that they represent both an ultimate limitation and, potentially, an opportunity for MEMS devices as they approach the nanoscale.

## 2 Classical optical forces

Researchers have long pursued the use of electromagnetic waves to induce mechanical motion. Kepler was the first to hypothesize that solar radiation is responsible for the deflection of comet tails away from the sun. By 1903, Lebedew [10] and Nichols and Hull [11] had proved Maxwell’s hypothesis that light impinging on a thin metallic disk in vacuum would induce measurable motion. Over the course of the next century, applications for harnessing the energy of light were seen in systems ranging from “Solar Sails” and accelerators [12] to optical traps and tweezers [3, 13–15]. In the last decade, interest in near-field optical interactions has steadily increased, as on-chip optical circuitry has presented viable alternatives to slower electronic systems. The initial single-beam trapping experiment by Ashkin et al. [3] was the first to demonstrate the usefulness of optical gradient forces for the manipulation of macroscopic objects: a tightly focused laser beam can trap a spherical dielectric particle in both normal and tangential directions by balancing the scattering and gradients forces acting on the particle. Subsequent experiments demonstrated laser cooling and trapping of ions and neutral atoms [16–19], leading to breakthroughs in various aspects of atomic physics, including the realization of Bose-Einstein condensates [20, 21], quantum simulation of arrays of atoms trapped in optical lattices, and a new field of atom optics [22]. The physics of optomechanics has a strong resemblance with Doppler cooling in atomic/optical physics [23–25], whose groundbreaking development preceded optomechanics by two decades, except that in optomechanical systems the predicted quantum nature is manifested in macroscopic objects. Instead of the atomic energy levels being dressed due to strong light–atom interactions, in optomechanics, the photonic resonant states are dressed due to strong optomechanical interactions. In addition to dynamical effects, optomechanical forces also lead to nano- and micro-meter mechanical displacements with milliwatts or smaller incident powers. Similar to conventional optical trapping, optical forces in optomechanical systems can be categorized into radiation, gradient, or photothermal forces. In the following sections, we briefly review the basic physics of gradient optical forces in micron-scale systems and survey recent developments paving the way toward designable interactions in a wide range of optomechanical systems, where the amplitude, wavelength, and phase of incident light can be used to obtain tunable attractive and repulsive forces.

### 2.1 Radiation, gradient, and photothermal forces

Radiation pressure involves transfer of momentum via propagating waves to a compliant object. While a photon carrying momentum $\hbar\omega/c$, or alternatively incident light carrying power $P$, is bounded by momentum conservation to contribute net pressure $\leq 2P/c$ (assuming 100% of the light is reflected from the object), the small momentum imparted by the photon can be drastically enhanced by introducing an optical cavity. Assuming negligible lossses, the force on any individual part of a cavity can be many times larger than the net force on the cavity as the photon continues to exchange momentum with it over the cavity lifetime $\tau$, thereby enhancing the force by a factor of $\tau$. The canonical example of such radiation-pressure enhancements in optomechanical systems is a simple Fabry-Perot cavity formed by two highly reflective mirrors in which one of the mirrors is allowed to move, leading to a number of observable mechanical effects [44]. Demonstrations of radiation pressure enhancement based on this principle cover a wide spectrum of length scales and designs, from large-scale mirrors and Fabry-Perot cavities formed by highly reflective Bragg gratings Fig. 1(i) to micron-scale whispering gallery modes Fig. 1(j) of microring resonators [45], where light circulates along the circumference of the cavities. The increasing demand for compact systems with smaller features has led to designs with increasing complexity and functionalities, including omnidirectional photonic-crystal (PhC) waveguides operating near band edges leading to slow group-velocity modes [46], PhC membranes with ultra-large mechanical lifetimes [47], parallel metallic-plate systems operating in the microwave regime [48], electrostrictive forces arising from strain-dependent refractive index changes [49], and even situations involving exotic materials such as left-handed materials [50] and gain media where the force can pull instead of push objects [51]. Designs tailored for applications in optomechanical systems often involve structures with co-localized optical and mechanical modes Fig. 1(k), where the combination of large optical quality factors $Q$ (dimensionless lifetimes in the range of tens of thousands or above) and long-lived mechanical modes (with frequencies in the MHz-GHz) have enabled exciting and novel demonstrations of optical spring effects, optomechanically induced self-oscillations, on-chip storage and manipulation of light pulses [52] and noise [53], on-chip accelerometers [54], microfluidic sensors [55], and cooling of macroscopic objects [23, 25, 56–61].

Gradient forces involve interactions induced by incident evanescent or gradient electromagnetic fields. In optomechanical systems, the most explored of these interactions is the force induced on a microcavity by the evanescent field of a nearby waveguide or substrate, where similar to radiation pressure, the forces are also greatly enhanced by resonances [62]. These include microcavities coupled to waveguides [59, 63], free-standing slot waveguides leading to wideband tuning and low-power optical modulation [64–66], PhC nanobeam waveguides coupled to substrates leading to unusual, non-monotonic attractive forces [67], zipper-like structures leading to optically controlled mechanical transparency [68–71], hybrid plasmonic waveguides leading to deep subwavelength confinement of light [72, 73], and plasmonic nanobeams [33, 74] or bowtie antennas [75], some of which are illustrated in Fig. 1. Tunable optomechanical interactions enabled by large gradient forces [62, 76, 77] are currently being explored in applications ranging from optical cooling [31], optical buffers [34], re-configurable filters [28], non-interferometric signal transduction [70, 78], and optical actuators and switches [79–82]. The interaction between coupled resonances through their evanescent field can lead to even richer phenomena, such as tunable attractive (bonding) and repulsive (anti-bonding) gradient forces between nearby optomechanical objects. The ability to generate repulsive forces and to tune the sign and magnitude of these interactions by adjusting either the wavelength or phase of incident light is also poised to make an impact in future photonic switching [83] and MEMS devices, where they could be exploited in conjunction with other forces such as Casimir or electrostatic forces (as described in Section 3.3).

Finally, light can lead to mechanical deformations through photothermal interactions, whereby a movable structure absorbs part of the incident light that is converted to heat. For instance, thermal stresses can arise in suspended devices as a result of the difference in thermal expansion coefficients between the device layer and underlying supporting substrate [84], leading to bending of the movable structure. Such photothermal deformations can often be enhanced by the introduction of a microcavity. Examples illustrated in Fig. 1(l) include a gold-coated silicon cantilever excited by a gold-coated optical fiber placed in close proximity, forming a Fabry–Perot cavity [43], and a cavity formed by a cantilever and neighboring substrate, excited with a laser frequency above the silicon bandgap [42]. While the photothermal effect also allows for optical spring tuning and dynamic back-action (mediated by delay due to its finite thermal time constant), the photothermal effect often presents itself as a competing effect in the demonstration of several optomechanical devices [36, 43, 85–89].

### 2.2 Designer bonding and antibonding forces

Among the successes of optomechanics is unprecedented access to quantum regimes of macroscopic

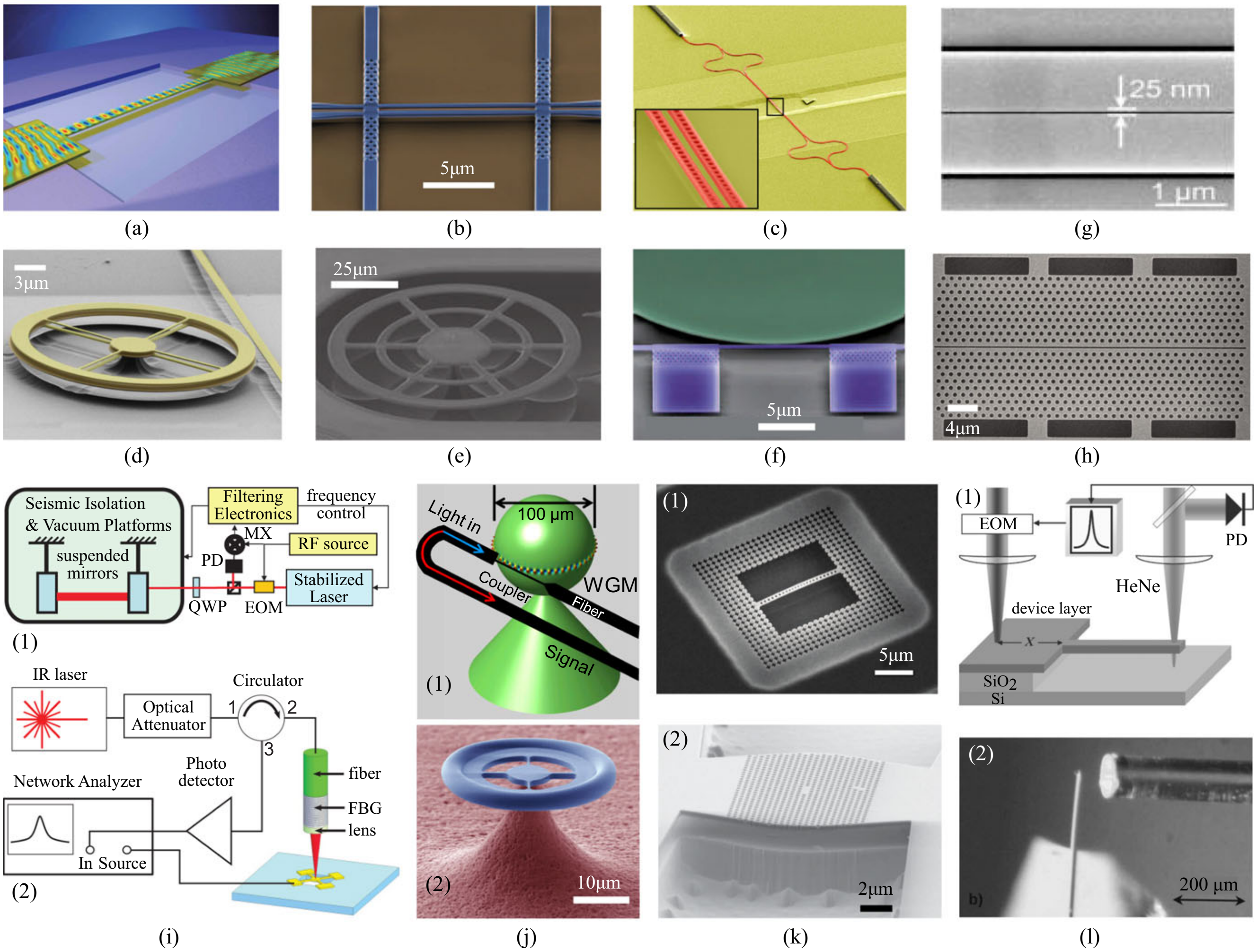

**Figure 1** Selected optomechanical structures actuated by radiation, gradient, and photothermal forces. Gradient-based designs include: (a) A silicon waveguide acting as a doubly-clamped beam coupling light incident from the underlying buried oxide layer, exhibiting attractive, lateral gradient forces and Duffing nonlinearities [26]. (b) Coupled silicon waveguides where attractive and repulsive optical forces are exerted by controlling the relative phase of incoming light via a Mach-Zehnder interferometer [27]. (c) Coupled silicon PhC nanobeam cavities where attractive optical forces are observed in the presence of incident incoherent light under atmospheric conditions [28]. (d) Coupled silicon-nitride ring resonators and silica microdisks supporting whispering gallery modes leading to attractive and repulsive forces [29–31]. (f) Dispersive and dissipative reactive forces realized in a system of silicon waveguides coupled to a silicon microdisk [32]. (g) Gold-coated silicon nitride plasmonic waveguides [33] and (h) silicon PhC slot-waveguides [34] exhibiting tightly confined electric fields inside the small air gaps. Radiation-based designs include: (i-1) Fabry–Perot cavities formed by large, kg-scale mirrors suspended by pedulums operating at very high powers and exhibiting optical instabilities [35]. (i-2) High-finesse Fabry-Perot cavities formed by gold-palladium rectangular mirrors [36]. (j-1) Silica microspheres supporting optical and acoustical whispering gallery modes where excitation of mechanical modes is facilitated by stimulated Brillouin scattering [37, 38]. (j-2) Silica microtoroids supporting whispering gallery modes used to demonstrate coherent quantum coupling [39]. (k-1) Silicon optomechanical crystals with phononic shields that have been optomechanically cooled to the quantum ground state [40]. (k-2) InP photonic crystal cavities designed to have strong localization of both optical and mechanical modes [41]. Photothermal-based designs include: (l-1) Silicon cantilevers actuated by thermal stress induced by absorption of visible HeNe light [42]. Here, the photothermal effect is modulated by a Fabry-Perot cavity formed by the silicon cantilever and the bottom silicon substrate. (l-2) Combination of radiation pressure and photothermal effects manifested in an optomechanical system comprised of an optical fiber above a reflective gold-coated silicon cantilever [43].

objects, most commonly realized in singly resonant optomechanical structures [39, 40, 90]. Other endeavors for expanding the optomechanical toolbox are noteworthy as well. In the next few sections, we present a number of recent theoretical and experimental studies which highlight the breadth of designs and functionalities in coupled, resonant optomechanical systems subject to bonding and antibonding forces.

### 2.2.1 Theory

To illustrate the origin of optical gradient forces between resonant optomechanical systems we begin by considering one of the first proposed optomechanical structures exhibiting this effect, involving two square dielectric waveguides placed in close proximity [91]. In such a system, the mutual interaction of degenerate resonances or guided modes via their evanescent fields can induce a splitting of the modes into pairs characterized by attractive and repulsive mechanical forces, analogous to the well-known bonding and anti-bonding states formed by the level splitting (avoided crossings) of interacting degenerate states in quantum systems [93]. The degree of mode splitting from the initial mode frequencies is controlled by the coupling strength (or proximity) between the waveguides [91, 94]. The idea is illustrated in the dispersion diagram of Fig. 2(a), which shows changes in the frequency dispersion of the two waveguide modes as they approach one another from infinity [91]. The relationship between changes in the frequency and mechanical energy of the system can in turn be understood from a simple, heuristic, quantum-mechanical argument [91]. In particular, assuming that $N$ photons of frequency $\omega$ and conserved wavevector are coupled into the waveguide system, the photonic energy $U$ can be written as,

$$U = N\hbar\omega, \tag{1}$$

from which it follows that a small change in the separation will shift $\omega$ and result in an optomechanical force,

$$F_{\mathrm{om}} = -\frac{\partial U}{\partial d} = -\frac{\partial (N\hbar\omega)}{\partial d} = -\frac{U}{\omega}\frac{\partial\omega}{\partial d} \tag{2}$$

acting on both waveguides. As expected, the final expression for the force does not depend on $\hbar$ but rather on the total stored energy in the system and can be derived and verified via classical arguments [95–97]. A useful figure of merit present in Eq. (2) is the so-called optomechanical coupling $g_{\mathrm{om}} = \frac{\partial\omega}{\partial d}$, which facilitates direct comparison of optomechanical forces between different structures.

Mixing between the modes of the isolated waveguides as they come together causes a splitting in the frequency where, as expected from a simple tight-binding picture or from perturbation theory [93], they hybridize into symmetric (lower frequency) and anti-symmetric (higher frequency) modes. Typically, when the guided waves are in phase (a bonding/symmetric mode), the electromagnetic energy can be reduced by increasing the field intensity in high-dielectric regions, leading to an attractive optical force that pushes the waveguides closer to one another. Conversely, when the guided waves are out of phase (an anti-bonding/anti-symmetric mode), the energy can be reduced by increasing the field intensity in low-dielectric regions, leading to a repulsive force. When mechanical degrees of freedom are introduced in these coupled structures, i.e. the waveguides are partially released from the bottom substrate, these optical forces push the waveguides in an effort to reconfigure the waveguides and hence lower the total energy. In this particular example, the polarity of the optical force is predominantly determined by the relative phases of the electric fields in the respective waveguides, which yields a control parameter to obtain tunable optomechanical effects, even switching the sign of the force from attractive to repulsive, an effect that was first observed experimentally in Refs. [27, 98]. Although the simple tight-binding picture above is sufficient to explain the main features of gradient forces at large separations $d \gg \lambda_p$, where $\lambda_p$ is a characteristic lengthscale corresponding to the exponential tail of the modes, at shorter separations $d \lesssim \lambda_p$ it can fail dramatically and one must therefore rely on exact calculations. These features are illustrated in Fig. 2(b), which shows the forces induced by both the bonding and antibonding modes of the waveguides over a wide range of separations. As observed from Fig. 2(b), the force scales exponentially with $d$ at large separations and exhibits a more complicated $d$-dependence at smaller separations. In this geometry, non-perturbative effects arising at short separations lead to a dramatic qualitative change in the behavior of the anti-symmetric mode, manifested as an increasingly weaker force with decreasing $d$ which ultimately switches sign (becoming attractive) below some threshold $d \lesssim 0.3a$.

Generalizations of this phenomenon to other coupled-cavity systems (e.g. microsphere, microdisk, and photonic crystal cavities) have paved the way for designable gradient forces. While most optomechanical structures often involve some kind of resonant effect, technically Eq. (2) is only applicable in closed systems comprising lossless (guided) resonances. In the presence of small losses, e.g. stemming from either radiation or absorption, similar formulas can be derived

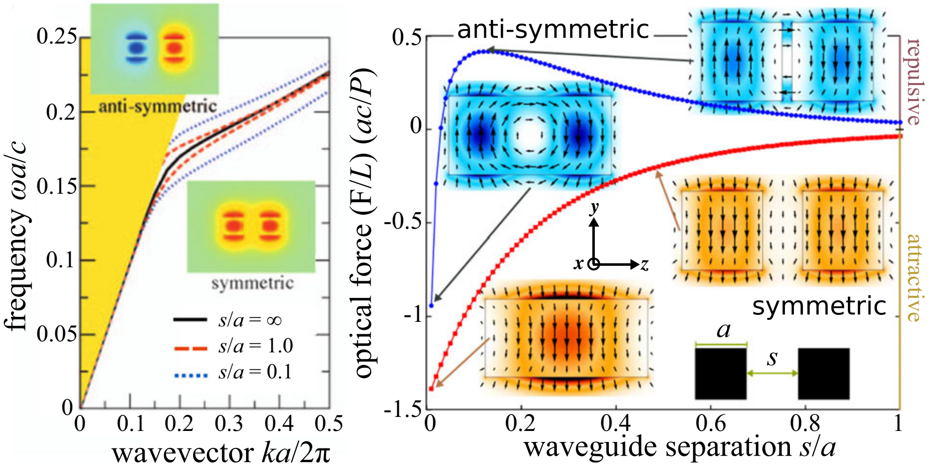

(a) (b)

**Figure 2** Working principles behind gradient forces in coupled optomechanical systems. (a) Dispersion diagram for a system involving two identical, co-planar square waveguides at various separations $s/a = \infty$ (black solid), 1 (red dashed) and 0.1 (blue dashed), where $a$ denotes the waveguide width [91]. Insets show the $E_y$ electric-field profile of both bonding (symmetric) and anti-bonding (anti-symmetric) modes. As $s$ decreases, the bonding and antibonding mode-frequencies experience red and blue shifts, respectively. (b) Normalized gradient force per unit length and per incident power for the same system, as a function of $s$ (for a fixed incident wavevector), where $+/-$ corresponds to repulsive/attractive forces [92]. Insets show the in-plate electric-field vectorial distribution and total intensity of both bonding and antibonding modes. The force amplitude of the bonding mode increases monotonically with decreasing $s$, whereas the anti-bonding force is only repulsive at separations $s/a \gtrsim 0.03$, becoming attractive at short distances.

(independent of the quantum-mechanical picture above) which relate forces to the frequencies, incident power, and lifetimes of the corresponding leaky modes [63, 95, 97]. In more general circumstances where there may not be well-defined resonant modes with negligible loss, or situations where there are superpositions of resonant modes with other waves (e.g. light from an external source), modal approaches become problematic. However, because optical forces are directly related to the solution of scattering problems, i.e. electromagnetic fields due to incident currents or fields, one can also frame the calculation of forces using formulations that do not rely on either mode or energy calculations and which generalize to other situations of interest, e.g. non-resonant or broad-bandwidth excitation, and even optical torques [14]. One such approach involves computing the force via the integral $\vec{F} = \oint \langle \vec{T} \rangle \cdot d\vec{S}$ of the time-averaged Maxwell stress-tensor,

$$T_{ij} = \frac{1}{2}\Re\left[\varepsilon_0\left(E_iE_j - \frac{1}{2}\sum_k |E_k|^2\right) + \mu_0\left(H_iH_j - \frac{1}{2}\sum_k |H_k|^2\right)\right] \tag{3}$$

around some surface $S$ lying in vacuum [2]. Calculation of stress tensors between vacuum-separated bodies sidestep issues relating to evaluation of energy densities in lossy media[1] and have been performed in a variety of contexts. For instance, $\langle \vec{T} \rangle$ can be directly computed via eigenmode calculations in systems with negligible loss [99, 100], or more generally by solving a set of linear equations for the fields in the frequency domain via finite differences, boundary or finite elements, and transfer-matrix methods [74, 101–104]. If a broad-band force spectrum is desired, one can also compute stress tensors via the Fourier transform of a short pulse in the time domain, yielding the entire spectrum at once [94]. Modern numerical methods based on the surface-integral equation formulation of electromagnetic scattering sidestep altogether the need to integrate stress tensors over bounding surfaces (which can lead to numerical problems) or computations of scattered fields, and instead express the force (or torque) via compact trace formulas that involve the solution of well-studied linear systems from the boundary-element method [105]. Ultimately, since incident light is often introduced over a narrow range of frequencies,

---

[1] Evaluation of either energy or stress tensor in dissipative media can be problematic [2]. However, since most cases of interest involve bodies separated by vacuum, these issues can generally be ignored.

calculations can be performed expediently and for arbitrarily complicated structures. As discussed in Section 3.1, similar numerical techniques have been developed for computations of fluctuation forces, where the significantly larger number of radiating centers and bandwidths complicate matters.

### 2.2.2 Recent developments

Since the first demonstrations of attractive and repulsive optical gradient forces between either a silicon waveguide and a silica substrate [26] or two silicon waveguides [98], a deluge of optomechanical structures actuated by resonantly enhanced optical gradient forces rapidly emerged. Geometries and materials explored to attain optomechanical transduction and actuation involving coupled resonances range from silica and GaAs microdisks [30, 45, 106], silicon nitride microrings [29], and more recently silicon and InGaAsP photonic crystal (PhC) membranes and cavities [28, 103, 107–111]. Each coupled system has its own competitive edge depending on the desired application, e.g. choice of mechanical modes suitable for atmospheric operations, choice of materials for thermal power handling, considerations based on the coupling mechanism or bandwidth requirements, etcetera, but most designs share the general feature of frequency-dependent polarity of gradient forces. Similar to level repulsion in guided modes of coupled waveguides, resonances with finite lifetime, be they whispering gallery modes, guided resonances in one and two-dimensional photonic crystals, or localized modes in PhC cavities, split into attractive and repulsive force pairs upon evanescent coupling, enabling actuation of devices by choosing the corresponding excitation frequencies.

A commonality of current demonstrations of coupled optomechanical devices is the strategy of tailoring and enhancing optical interactions. Since the strength of the optical force is related to the change in optical energy with respect to mechanical deformations, techniques of resonantly enhancing light–atom interactions in photonic chip-based systems were immediately translated to boost the coupling and force amplitude of optomechanical systems [112–116]. New directions of enhancing the transverse attractive and repulsive gradient forces, apart from the typical approach of employing ultrahigh-$Q$ optical modes in microspheres or ring resonators [30, 95, 106, 117–119], have emerged in recent years. Some of these strategies are illustrated in Fig. 3 and include: adopting slow-light Bloch modes to enhance the intra-cavity optical energy [120], designing more complex morphologies to engineer the field distributions near the interacting surfaces [121, 122], and incorporating metamaterials that locally engineer the dielectric profile experienced by the evanescent field in the vicinity of the nearby objects [123, 124], or which effectively reduce the coupling distance perceived by the fields, thereby ameliorating the challenge of fabricating free-standing devices with thin sacrificial layers [125].

Forces between coupled waveguides have been studied in a variety of planar structures [96, 99, 126], including finite and infinitely thick metal slabs where surface plasmons mediate the interaction, but whose magnitudes are ultimately limited by high losses [100]. Spoof plasmons involving sub-wavelength corrugations on the surface of a semi-infinite metal have also been explored, demonstrating strong gradient forces at lower frequencies where losses tend to be smaller [127]. However, most of these systems suffer from limitations similar to those of the original silicon waveguide geometry of Ref. [91], namely the strength of the repulsive force is bounded. While the attractive force of a bonding mode monotonically increases in strength as the two resonant systems approach one other, an antibonding mode is not guaranteed to generate a repulsive force [91]. For the above example of two square waveguides, the relatively large cross-sectional area and the absence of an air gap between the structures when touching have been identified as primary reasons for the transition from repulsion to attraction at short separations [92]. (The absence of an air gap at short separations means that the anti-bonding mode cannot continue to increase its frequency indefinitely [128].) Recent work by Oskooi et al. demonstrated that other waveguide cross-sections can reverse this trend, and in particular they consider waveguides with cylindrical and semi-circular cross-sections Fig. 3(a) whose convex inner surface maximize the presence of air regions as they come together. Even larger forces can arise in waveguide systems when operating near the band edge of a guided mode, e.g. induced by introducing a periodic grating along the invariant direction [128], due to the smaller group velocity of these modes. The combination of convex surfaces and slow-light modes induced by periodicity was shown to lead to orders of magnitude larger repulsive forces [92], as illustrated in Fig. 3(b).

Other recently studied planar-waveguide structures include metamaterials comprised of metals and dielectrics arranged into complex microstructures with sub-wavelength features [124, 125, 130–132]. For instance, by employing ideas from transformation optics, Ginis et al. describe a structure, a thin layer of double-negative metamaterial involving a double layer of split-ring resonators in dielectric on top of a dielectric

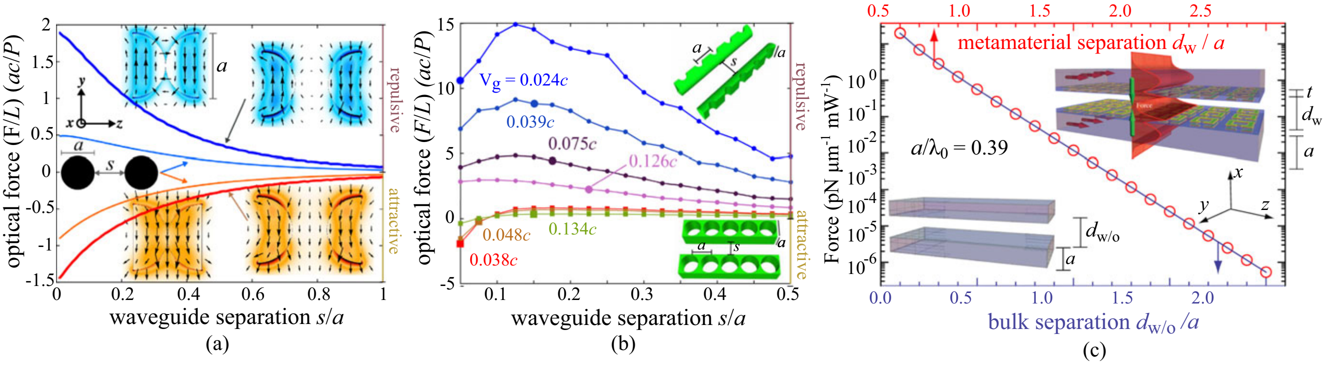

**Figure 3** Examples of recent approaches to modifying gradient forces between waveguides. (a) Normalized optical force as a function of separation $s$ for two waveguide structures consisting of either circular (thin lines) or semi-circular (thick lines) cross sections [121], showing that in contrast to square waveguides [Fig. 2(b)], repulsive forces increase monotonically with decreasing $s$. The explanation comes from continuity conditions and the fact that convex surfaces tend to better concentrate electric fields in low-dielectric regions, enabling the frequency of anti-bonding modes to continually increase with decreasing $s$. Insets show the in-plane electric-field vectorial distribution and total intensity of both bonding and antibonding modes. (b) Normalized anti-bonding force between coupled PhC waveguides with either square (squares) or semi-circular (circles) cross-sections, as a function of $s$. The slow-light characteristic of the modes (small group velocity $v_g$) enhances the force, an effect that is more prominent for semi-circular cross-sections. (c) Slab waveguides cladded with a thin metamaterial layer composed of split-ring resonators (top inset), designed to reduce the effective distance perceived by the evanescent field of interacting modes and leading to force enhancements of more than an order of magnitude [125]. Plot shows the gradient force in the absence (blue line) and presence (red circles) of the metamaterial layers, designed such that their separation $d_{\mathrm{w}} = d_{\mathrm{w/o}} + 0.5a$, where $d_{\mathrm{w/o}}$ and $a$ are the separation and thickness of the bulk (unpatterned) slabs.

substrate, which allows significant reduction of the effective optical space between two waveguides [125]. The design and results are presented in Fig. 3(c–d), which illustrate large enhancements in the bonding force between the two waveguides. Another class of artificial structures that show great promise are magnetoelastic or optomechanical metamaterials, in which gradient forces between movable elements forming the metamaterial lattice enable on-demand changes in the metamaterial structure or lattice [124, 131]. Such optomechanical interactions between "microscopic" elements were explored by Lapine et al. in an anisotropic magnetic metamaterial structure involving elastic split-ring resonators, demonstrating strong nonlinear and feedback effects, e.g. hysteresis, arising from optomechanically induced changes to the bulk metamaterial properties of the system [131]. These systems present enormous potential for nonlinear, reconfigurable devices with self-adaptive photonic functionalities [124]. More recently, the effect of non-locality due to gradient forces mediated by surface-plasmon polaritons in a wire-based metamaterial medium was explored [132].

Gradient forces can also be greatly enhanced by planar surfaces nanostructured at the scale of the incident wavelength, such as those observed in PhC slabs and microcavities, leading to enhanced gradient forces over significantly larger areas compared to similar 1d waveguide structures. For instance, the force between ultra-thin and high-$Q$ microcavities in PhC membranes was recently shown to lead to significant optomechanical wavelength and energy conversion [107, 108, 133]. Moreover, the in-plane periodicity of PhC membrane structures gives rise to leaky resonances [128] that couple to externally incident radiation and which can lead to strong bonding and antibonding forces [103, 129]. Another notable approach of force enhancement can be found in exploiting symmetry in such extended periodic structures: by breaking periodicity in PhC gratings or nanobeams (e.g. by perturbing the alignment of periodic holes), ultra-large normal and lateral forces can be engineered [103, 122, 129, 133]. The idea, first explored by Liu et al., relies on the existence of certain leaky modes, or "bright" guided modes of isolated, unstructured slabs that can couple to external radiation via the periodicity (band folding), which due to symmetry cannot couple to external radiation [129]. While such "dark states" have vanishing bandwidths (infinite lifetimes) in isolated PhC membranes, they can acquire finite lifetimes (coupling to external radiation) when the two PhC slabs come into close proximity, as illustrated in Fig. 4. Specifically, when two such slabs are evanescently coupled, two interesting phenomena can occur: First, in the vicinity of certain separations $d_\infty$, the Fabry–Perot-like interference of bright modes can form high-$Q$ dark states. Second, by breaking the

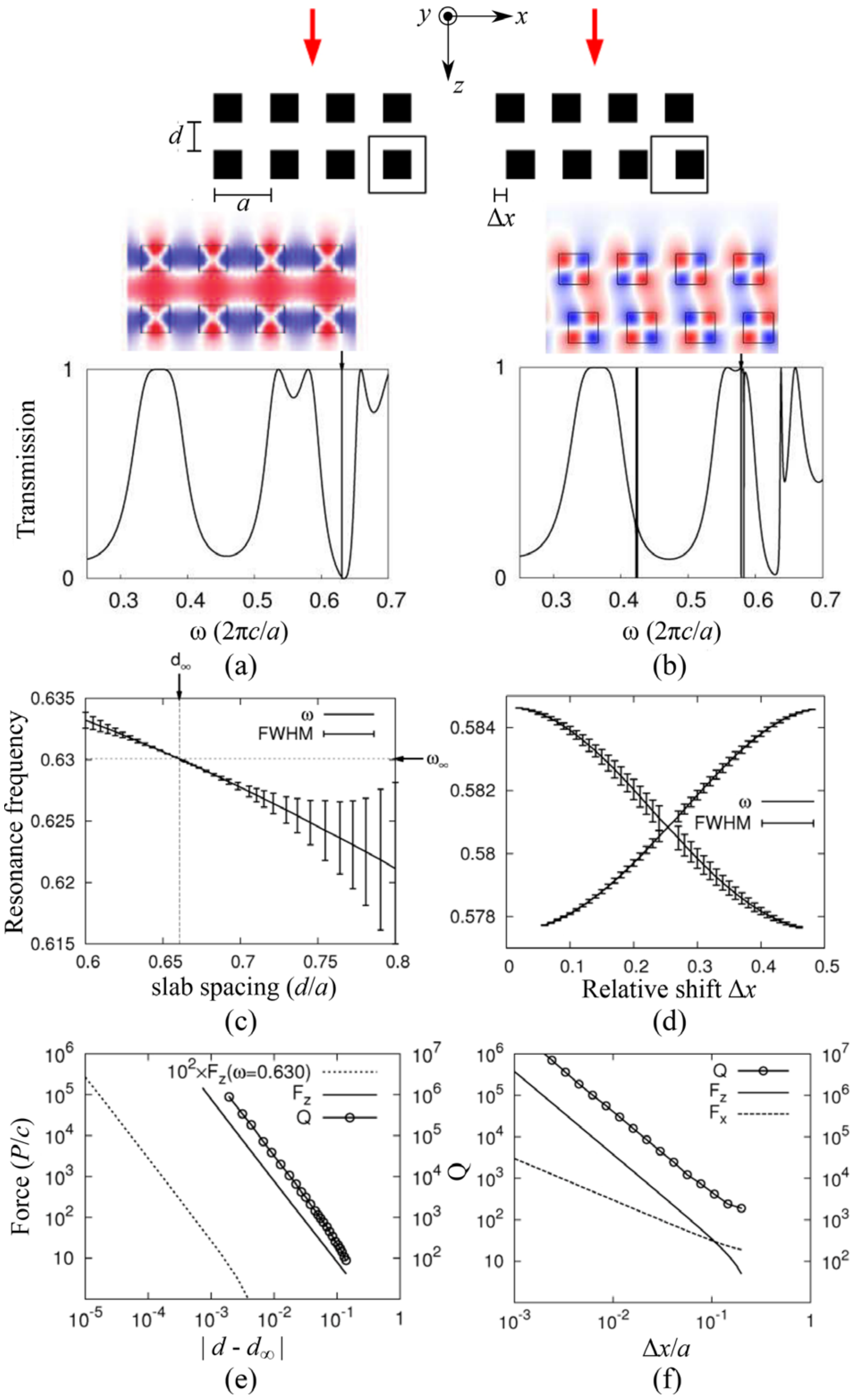

**Figure 4** Predictions of ultra-large normal and lateral gradient forces in PhC membranes mediated by dark modes [129]. Transmission spectrum of the system for two different configurations of membrane separations $d$ and lateral translations $\Delta x$, (a) $d = 0.65$, $\Delta x = 0$ and (b) $d = 0.5a$, $\Delta x = 0.15a$, along with the mode profiles of two corresponding high-$Q$ dark states appearing at $\omega = 0.63\ (2\pi c/a)$ and $\omega = 0.58\ (2\pi c/a)$, respectively, where $a$ is the membrane period. The dark modes arise due to either (a) Fabry–Perot-like interference effects or (b) broken symmetry. (c) and (d) show the resonance frequency and linewidth of the dark modes in (a) and (b) as a function of $d$ and $\Delta x$, respectively. As shown, at $d_\infty$ the membranes do not couple to external radiation. (e) and (f) show the corresponding variations in the normal ($F_z$) and lateral ($F_x$) forces, and $Q$ for light incident either on (solid line) or slightly detuned (dashed line) from resonance (solid line).

mirror symmetry of the system, e.g. via a lateral shift of one of the slabs relative to the other, dark states that otherwise could not couple to external radiation by symmetry are allowed to. As shown in Fig. 4, the presence of such "nearly dark" modes leads to tunable longitudinal and lateral forces on the slab. The versatility of actuation and sensitivity of transverse and lateral optical forces could potentially be employed as an all-optical three-dimensional accelerometer.

Attractive and repulsive force pairs also arise in highly asymmetric planar systems, such as in the system considered by Ref. [94] and shown schematically in Fig. 5(a), consisting of a silicon PhC membrane coupled to a layered silicon-on-insulator substrate. Here, in contrast to symmetric PhC membranes, the periodicity of the PhC membrane induces coupling between the lossy (finite lifetime) leaky resonances of the membrane and the lossless (infinite lifetime) guided modes of the silicon-on-silica system. As shown in Fig. 5(a), level repulsion arises even when the non-degenerate modes of the two slabs approach one another (although degenerate modes can also be designed), leading to bonding and antibonding forces. Two interesting features stemming from the asymmetry are highlighted here: First, from the mode profile illustrated in Fig. 5(b), the bonding mode bears more resemblance to the slab waveguide mode while the antibonding mode bears more resemblance to the leaky PhC guided resonance. Consequently, the bandwidth (lifetime) of the bonding mode has a significantly stronger dependence on the slab separation Fig. 5(b), going from $Q = \infty$ at $d = \infty$ to a finite value $Q \approx 10^2$ at shorter separations. Second, as a result of the strong coupling-dependent variation in $Q$ of the bonding mode, while the repulsive force (antibonding mode) increases in strength as the membrane separation decreases, the attractive force (bonding mode) amplitude decreases, as shown in Fig. 5(b), in contrast to what is normally observed in most mirror-symmetric systems. A related structure, involving a nanostructured membrane on top of a substrate, was recently studied in the metamaterial limit where the membrane consisted of a plasmonic metamaterial [123].

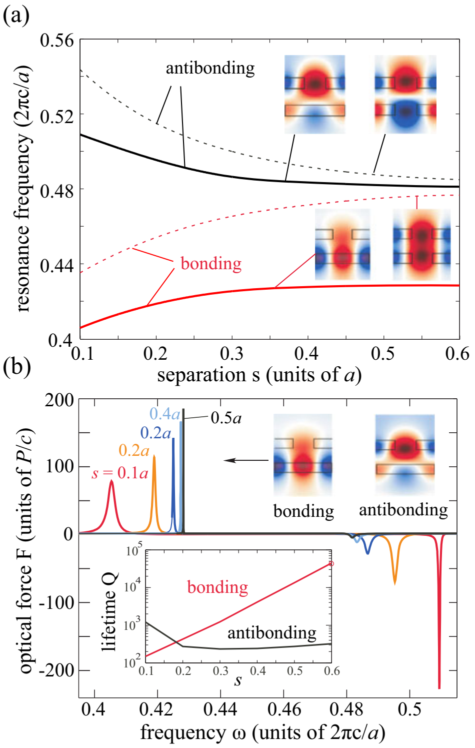

**Figure 5** Working principles behind gradient forces in asymmetric membrane geometries. (a) Resonant frequencies (units of $2\pi c/a$) of both symmetric PhC–PhC (dashed lines) and asymmetric PhC–slab (solid lines) membrane structures of period $a$, as a function of membrane separation $s$. Bonding (red) and anti-bonding (black) modes are excited by normally incident light from above. Insets show the $E_x$ electric-field component for a cross-section near resonances at a single $s = 0.3a$, delineating the in- and out-of-phase characteristics of bonding and anti-bonding modes, as well as the asymmetric concentration of energy in the PhC–slab structure. (b) Force spectrum of the asymmetric structure for multiple PhC-slab separations, obtained via the Fourier transform of a short-pulse excitation in time [94]. Inset shows the corresponding quality factor $Q$ as a function of $s$, illustrating the dramatically different behavior of bonding versus anti-bonding modes.

A recent experimental demonstration of repulsive forces that captures many of the design principles discussed above involves the asymmetric structure shown in Fig. 6(a–b), featuring a tethered silicon PhC membrane of size 30 $\mu$m $\times$ 30 $\mu$m suspended above a typical silicon-on-insulator (SOI) substrate [89, 134]. Specifically, the optomechanical properties of the structure were probed and actuated with a band-edge dark resonance, whose in-plane symmetry and field (phase) profile are illustrated in Fig. 6(b), leading to a repulsive force in the telecom range. In contrast to approaches based on mirror-symmetric bodies, experimental access to the dark mode in the asymmetric system was made possible due to the finite size effect of the membrane as well as fabrication-induced inhomogeneities, resulting in significantly lower lifetimes $Q \approx 4400$ than some of the other recently studied structures, featured in Table 1. For vertically coupled optomechanical devices like those shown in Fig. 1(d–e), tunability of the optomechanical coupling strength is not well controlled or would otherwise require a new substrate with different sacrificial layer thicknesses. As shown in Fig. 6(d), wide-range tuning of the

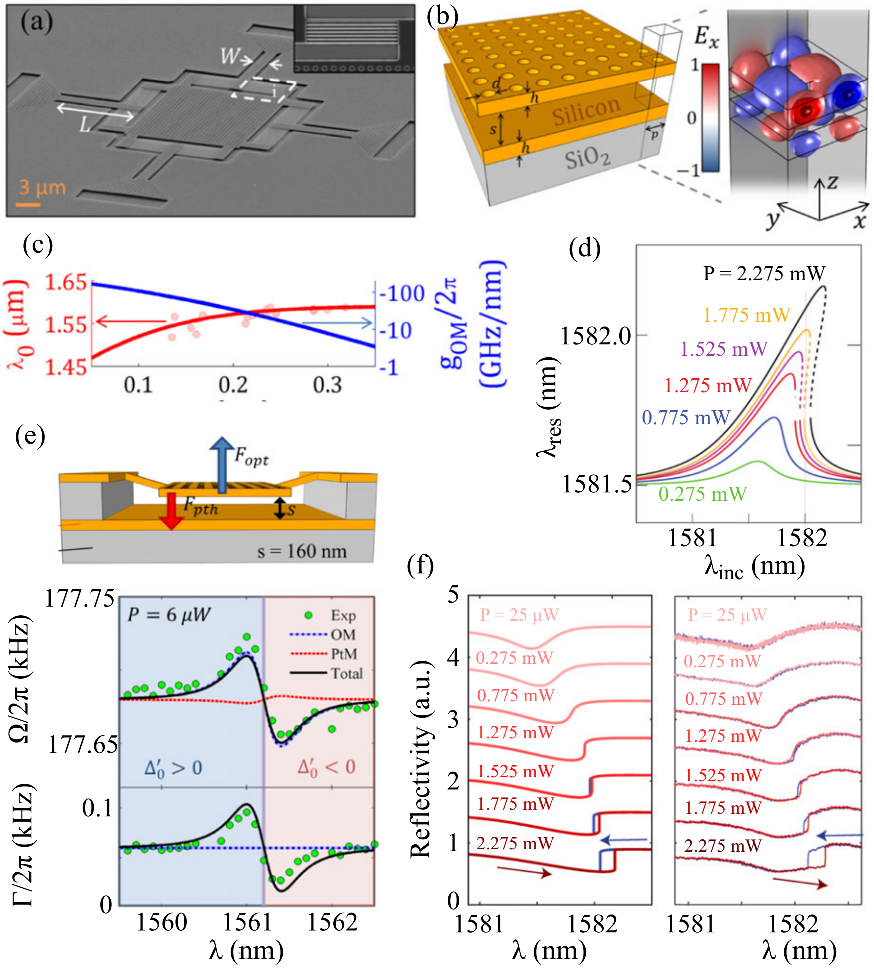

**Figure 6** Experimental demonstration of dark-mode repulsive forces in PhC membranes [134]. (a) Electron micrograph of device consisting of a silicon PhC membrane suspended above a silicon-on-insulator substrate, shown schematically in (b). The membrane is a $27.6\ \mu\text{m} \times 27.6\ \mu\text{m}$ slab of thickness $h = 185$ nm perforated by a 30×30 array of holes with diameter $d = 0.414\ \mu\text{m}$ and period $p = 0.92\ \mu\text{m}$. Also show is the $E_x$ electric field profile of an anti-bonding dark mode at the incident wavelength $\lambda = 1581.55$ nm. (c) Calculated (solid lines) and measured (pink circle) resonance wavelength (red) and optomechanical coupling $g_{\text{om}}$ (blue) of the dark mode as a function of the PhC–slab separation $s$. (d) Resonance wavelength as a function of incident laser power $P$ and wavelength, for six values of $P$. At a certain critical power $P_{\text{bis}} \approx 1.275$ mW, the system exhibits bistability stemming from optomechanical and photothermal effects, displaying hysteresis beyond a threshold power $P_{\text{hys}} \approx 1.525$ mW as the laser wavelength is continuously swept backwards (blue line) and forwards (red line), as evidenced by the theoretical (1) and experimental (2) reflection spectra in (f). (e) Schematic illustration of the competing optomechanical and photothermal forces on the membrane, along with the measured mechanical frequency $\Omega_m$ and decay rate $\Gamma_m$ of the fundamental mechanical mode across the optical resonance at incident power $P = 6\ \mu$W. Experimental data is fitted to predictions from theoretical models based on the coupled-mode theory framework [134].

optomechanical coupling strength in the range $g_{\text{om}} = -2\pi \times (5, 66)$ GHz/nm was achieved on the same substrate by engineering the in-plane compressive stress of the silicon device layer and the stress-gradient-induced torque, enabling control of the separation between the membrane and substrate in the range of 120–300 nm. In addition to exhibiting both optical spring effects and dynamic back-action Fig. 6(e), the system was shown to exhibit blue-detuned cooling and red-detuned amplification, in contrast to what is normally observed in conventional optomechanical systems. Such unusual effects are a manifestation of the interplay between photothermal and optomechanical forces. Moreover, optical bistability is observed as a result of both optomechanical dispersion and thermo-optic effects Fig. 6(f), occurring whenever the membrane transitions from one

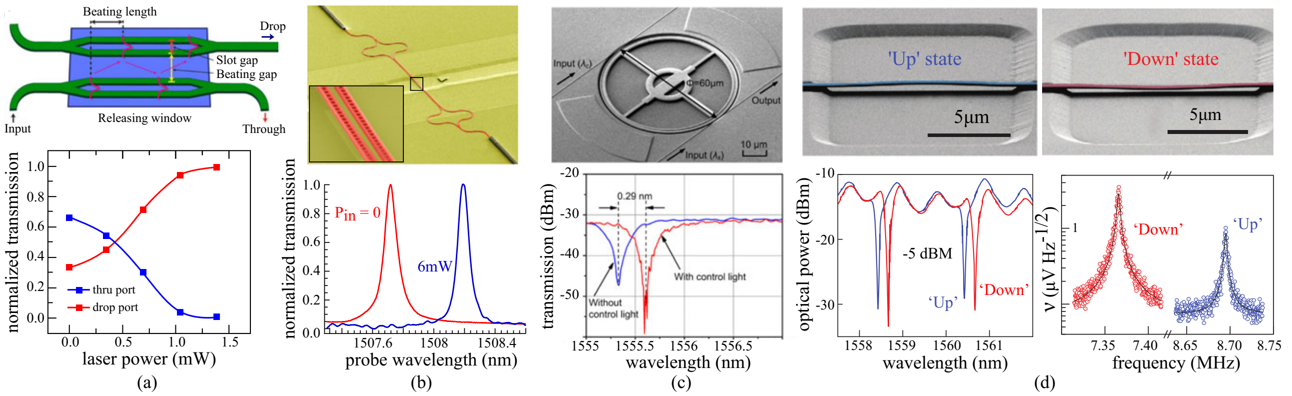

**Figure 7** Selected applications of experimentally realized optomechanical systems exploiting gradient forces. (a) Optical waveguide couplers where on-chip tuning is achieved by strong optomechanical coupling in silicon slot waveguides [64]. Plot shows static tuning of the through (blue) and drop (red) port transmissions as a function of incident laser power at two different probe wavelengths. (b) Coupled photonic crystal nanobeam cavities employed as an all-optical tunable filter that can be actuated with incoherent light sources [28]. Plot shows tuning of the cavity resonance via thermo-optic, free-carrier, and optomechanical effects induced by incident power at 0 (red) and 6 mW (blue). (c) Optomechanical switching with timescales on the order of tens of nanoseconds, where resonance tuning is achieved by controlling the coupling between a silicon resonator and an underlying buried oxide layer [82]. Plot shows a zoom-in view of the wavelength shift induced by the control light in either the off or on state. (d) Optomechanical memory involving bistable transitions induced by gradient forces [140]. Plots show the transmission (optical power) and thermomechanical $v_n$ noise spectra at low input powers when the resonator (shown schematically) is in the up (blue) or down (red) states. The 'up' and 'down' states enable the possibility of writing nanomechanical memory sequences.

mechanical equilibrium to another created by the optical potential.

Generally, photonic structures that support many resonances, e.g. microdisks, PhC slabs, and microspheres, will exhibit complicated force spectra due to the coupling-induced frequency-splitting among all modes, especially in the higher frequency range where the density of states increases. In combination with the complex interactions between lossless and leaky resonances arising in systems such as the asymmetric membranes above, these features shed light on new strategies for engineering resonantly enhanced gradient forces. For instance, it is possible to perform multimodal excitations to engineer the net optical force exerted on the optomechanical structure and thereby tune the mechanical spring constant dramatically without perturbing the initial mechanical equilibrium [94]. Simultaneous frequency excitations in systems with sub-micron dimensions can also create highly localized optical traps [94, 118], opening up new avenues of optomechanical trapping and even exposing the system's mechanical nonlinearity as the linear response is suppressed.

To summarize the various approaches of gradient force enhancement, Table 1 highlights some of the recently studied and representative gradient-force-actuated optomechanical devices, comparing their fundamental mechanical frequencies and quality factors, optical lifetimes, optomechanical coupling strength, and maximum force/mechanical amplitudes. One observation is that various material systems are chosen for considerations such as photothermal effect, free carrier excitation and stress management. Another feature is the successful demonstration of atmospheric operations of these optomechanical devices which circumvent the need for hermetic vacuum packaging useful in sensing applications. Finally, we note that the realization of optomechanical structures with greater design complexities demands more sophisticated fabrication techniques. We anticipate that micro-fabrication advancements, including the ongoing development and experimental demonstrations of metamaterials in the micron-scale and multi-layer thin-film assembly assisted by soft lithography [135–139], will continue to pave the way toward new demonstrations of pronounced force enhancements with optimized optical designs.

## 2.3 Technological Impact

The conspicuous expression of the optical force in nanophotonic devices facilitates new strategies for achieving reconfigurable and programmable optical devices [28, 30, 64, 82, 141], further advancing the nascent

Table 1 Representative optomechanical devices based on gradient forces along with several corresponding figures of merit, including typical mechanical separations, frequencies $f_m$ and quality factors $Q_m$, measured optical quality factors $Q_{opt}$, optomechanical couplings $g_{om}$ ($+/-$ denotes bonding/anti-bonding modes), optomechanical force amplitudes, and static/dynamic mechanical amplitudes. Entries marked by hyphens "-" denote missing data. Unless otherwise noted, measurements are in vacuum.

| Team | Structure – separation (nm) | Mechanical frequency $f_m$ (MHz) | Mechanical quality factor $Q_m$ | Optical $Q_{opt}$ | Coupling $g_{om}/2\pi$ (GHz/ nm) | OM force (nN/ mW) | Amplitude (nm/ mW) |
|---|---|---|---|---|---|---|---|
| Eichenfield et al. 2007 [59] | SiN disk resonator with tapered fiber – 702 nm | $1.93 \times 10^{-6}$ | – | $1.1 \times 10^6$ | – | −0.02 | −324 |
| Li et al. 2008 [26] | Si waveguide with SiO2 substrate – 360 nm | 8.87 | 1850 | – | – | 0.005 | 2 |
| Li et al. 2009 [27] | Laterally coupled Si waveguides – 100 nm | 17.05 | 5300 | – | – | -2.2 (1.1) | 9.6 |
| Rosenberg et al. 2009 [30] | Vertically coupled SiO2 ring resonator – 138 nm | 8.3 | 3.95 (in air) | $1.8 \times 10^6$ | 33 | -244 | – |
| Wiederhecker et al. 2009 [29] | Vertically coupled SiN ring resonator – 640 nm | 0.6 | 2 (in air) | $6.8 \times 10^4$ ($2.1 \times 10^4$) | 1.4 (2) | – | −20 (1) |
| Eichenfield et al. 2009 [61] | Laterally coupled SiN zipper nanobeam cavity – 120 nm | 8 | 11600 (50) (in air) | $3 \times 10^5$ | 123 | – | – |
| Roh et al. 2010 [109] | Bilayer InP PhC membranes – 200 nm | 1.8 | 2 (in air) | 700 (1600) | (44) | (−0.83) | (−0.26) |
| Deotare et al. 2012 [28] | Laterally coupled Si PhC nanobeam cavities – 70 nm | 8 | 17 (in air) | 15000 | 96 | −1400 | 0.025 |
| Woolf et al. 2012 [89] | Si PhC membrane coupled with an SOI substrate – 160 nm | 0.16 | 2000 | 3400 | −66 | 1.2 | 1 |

field of nano-optoelectro-mechanical systems (NOEMS). Among coupled optomechanical structures, recently demonstrated reconfigurable passive optical elements include couplers with a pair of coupled optomechanical slot waveguides [64], broadband all-optical filters that can be controlled by incoherent light [28], and optical switches based on either coupled microdisks [30] or waveguide–substrate platforms [82] exhibiting switching times on the order of nanoseconds. Thus far, despite the relatively large degree of actuation achieved by optical forces in nanophotonic devices, electrostatic actuation still outperforms optomechanics in the extent of actuation [141–143]. However in applications where operating environments are adverse to systems with metallization, an all-optical platform could still be desirable.

A subtle effect that the optomechanics community has dealt with in past years is buckling of the optomechanical devices caused by compressive stress in device layers, e.g. in typical silicon-on-insulator substrates [144, 145], gallium arsenide [146], and diamond [147]. Such compressive stresses cause deviations of the fabricated structures from the desired geometry. On the one hand, solutions to this problem include resorting to material systems with *tensile* stress (e.g. silicon nitride) [29, 148], depositing a thin layer of materials to compensate the stress [149], or developing structural stress-relief techniques [54, 145]. On the other hand, some recent proposals take advantage of the presence of buckling to create mechanical, bistable states for switching and sensing which basically eliminate the consumption of holding power. Examples include demonstrations of mechanical memory by Bagheri et al. [140], optical shock sensors [150], and optical switches [151]. The strong optomechanical strength of modern designs also offers high readout sensitivity of mechanical motion, even under atmospheric conditions where mechanical signals could still be detected above the noise floor in the presence of strong viscous damping. Some of the recent demonstration exploiting readout sensitivity hard to reach by conventional electromechanical schemes include broad-bandwidth accelerometry in optomechanical slot waveguides [54], particle detection with self-oscillating toroidal resonators in air [152], optical switches [82], optomechanical AFMs [153, 154], and microfluidic optomechanical sensing in liquid environments [55, 155]. There is also strong drive to seek applications of optomechanics in the classical and quantum regimes, particularly in the radio-frequency window. However, the design of optomechanical devices that operate in the GHz range and exhibit efficient optomechanical transduction is a highly non-trivial problem. For instance, there are significant endeavors to design structures that feature strong colocalization of photonic and phononic modes that maximize dispersive coupling [156–158] and which enable wavelength conversion (from telecom to telecom and telecom to microwaves) mediated by GHz mechanical modes in the sideband-resolved regime [107, 159–165]. Self-oscillating optomechanical oscillators for timing applications in the radio-frequency window are also explored with phase-noise suppression schemes incorporated to rival existing technology of crystal oscillators [53, 66, 166–172]. Finally, the miniaturization of devices based on optomechanical forces will necessarily lead to other important considerations stemming from other competing effects, including electrostatic and fluctuation forces, the subject of the next sections.

## 3 Fluctuation forces

As micromechanical devices enter the sub-micron regime, fluctuation-induced electromagnetic forces such as van der Waals or Casimir forces become increasingly important, leading for example to unwanted “stiction” between moving parts [173–176]. Unlike their classical analogue, these interactions have their origins in the quantum and thermal fluctuation of charges in bodies [5, 9, 175, 177–193] and hence persist even in the absence of external inputs. The volumetric and broadband character of these fluctuations and their usually small nature makes design, calculations, and measurements of these forces significantly more challenging than their classical counterparts, although they can reach atmospheric pressures at nanometric separations. Theoretical calculations and experimental measurements were until recently limited to planar or nearly-planar structures, where forces are usually attractive and monotonically increasing with decreasing separation. Recent theoretical and experimental progress, however, is making it possible to study the ways in which geometry and materials affect both the sign and magnitude of these interactions, paving the way for potentially new design principles to enter micromechanical and microfluidic devices. In the following sections we review the basic physics of Casimir forces, describe the similarities and differences with classical optical forces and discuss recent design principles and experiments that probe the strong material and geometry dependence of the force, including predictions of repulsive or unusual interactions between microstructured surfaces. Finally, we discuss recent progress toward measuring and designing Casimir forces in integrated and optomechanical devices in which classical forces are used to actuate as well as combat stiction. For other recent reviews, the reader is encouraged to look in Refs. [9, 175, 189–196].

### 3.1 Casimir forces

The early studies of EM fluctuation forces dates back to the pioneering work of Johannes D. van der Waals, who predicted an attractive force between neutral atoms or particles stemming from quantum dipolar fluctuations [6, 197–199]. Such an interaction arises whenever a particle acquires a spontaneous dipole moment, either from quantum or finite-temperature fluctuations, producing a field that can polarize a nearby particle and lead to a corresponding dipole–dipole interaction [191]. The cumulative effect of such dipolar interactions over all frequencies are so-called “dispersion” forces that depend on both the separation and frequency-dependent polarizabilities of the particles, and which have come to be known as van der Waals forces in the near field (interactions dominated by evanescent fields) or Casimir–Polder forces in the far field (interactions dominated by radiative fields and retardation effects) [200]. Casimir forces are generalizations of this phenomenon to systems composed of many particles, such as macroscopic media [177], in which case the single-particle picture fails to capture important multiple scattering, boundary, and wave effects that can lead to strong modifications of the force laws.

In such situations, a different approach is needed, such as the framework introduced by Hendrik Casimir in 1948. In particular, rather than summing the energy contribution of dipoles within the macroscopic bodies, Casimir showed that it is equivalent to instead consider the energy stored in the corresponding (induced) electromagnetic fields. Within this formulation, the quantum-mechanical zero-point energy of the electromagnetic field can be related to the sum over modes of the system,

$$U = \sum_{\omega} \frac{1}{2}\hbar\omega, \tag{4}$$

where $\hbar$ is the reduced Planck's constant and $\hbar\omega/2$ is the energy of a virtual photon with frequency $\omega$. Application of Eq. (4) to Casimir's simplified model of two perfect electric-conductor (PEC) plates separated by a distance $d$, leads to the well-known formula for the pressure $P_{\mathrm{C}} = -\frac{\partial U}{\partial d}$ between the plates [5, 177],

$$P_{\mathrm{C}} = -\frac{\hbar c}{240\pi d^4} = 0.013\frac{1}{d^4}\mathrm{dyn}(\mu\mathrm{m})^4\mathrm{cm}^{-2}, \tag{5}$$

where $c$ is the vacuum speed of light. It follows that the force between the plates is attractive and monotonically increasing with decreasing $d$, a result that is often heuristically explained from the fact that the density of photonic modes is larger outside than inside the plates.

Because Casimir and classical forces are both related to the mode frequencies of a system, in principle one can employ classical ideas from nanophotonics to gain intuition. However, the similarities between Eq. (4) and Eq. 1 in Section 2.2.1 belie a number of fundamental differences that lead to dramatically different physics and design principles. First, we should note that the use of photon number in the classical energy expression of Eq. (1) is merely a heuristic and convenient way of relating the energy stored in a given mode to its corresponding frequency, and of course the physical energy stored in the system arises not from fluctuations but from externally incident light. (In fact, as mentioned above, one can also derive the classical force expression without introducing any quantum-mechanical quantities [95].) In contrast, the contribution $\hbar\omega$ of virtual photons in Eq. (4) has a direct physical interpretation as arising from zero-point charge (and electromagnetic) fluctuations inside and outside the bodies, as opposed to any external sources. Hence the quantity $\hbar$ appears in the final expression for the pressure (Eq. (5)). Second, since the Casimir energy is a result of broad-bandwidth electromagnetic fluctuations, from electrostatic all the way to UV wavelengths where materials become transparent, Eq. (4) contains a sum over all frequencies. As a consequence, whereas designs based on classical forces often focus on resonant effects, looking at the energy or force contributions within a narrow frequency bandwidth can be very deceptive in the Casimir case.

To illustrate this point, Fig. 8 shows the Casimir force integrand as a function of $\omega$ for two semi-infinite gold plates. Note that the expression in Eq. (5) is obtained only upong taking the idealized limit of a perfect metal ($\varepsilon \to -\infty$).[2] Regardless of material considerations one finds that, while certain frequencies give attractive contributions, others give repulsion, and the overall sign is determined by a complicated cancellation between these effects. The sum-over-modes calculation for dielectric plates dates back to the original work by Van Kampen [202], who computed the force in the near field $d \ll \lambda_p$, where $\lambda_p$ is a characteristic wavelength which for metals corresponds to the plasma wavelength (typically in the ultraviolet range). In this quasistatic regime, the force law scales as $1/d^3$ whereas at large separations $d \gg \lambda_p$, the force again scales as $1/d^4$. In between, the $d$-dependence of the force is determined by the frequency-dependent permittivity $\varepsilon$ of the materials involved. This transition reveals the increasing contribution of evanescent waves in the near field, as recognized by Van Kampen. More recently, there has been renewed interest in analyzing the modal contributions at different frequencies and separations, which, just as in the classical case, can be classified as arising from either evanescent (gradient) or propagating (radiative) modes [201, 203, 204]. Such a decomposition was explored in Ref. [205], which found that evanescent modes not only dominate the interaction at small $d$, but also contribute a significant repulsive component at larger separations stemming from the contribution of antibonding modes, with bonding modes contributing attraction in analogy with classical forces. Ultimately, however, the sign and scaling of the force is determined by a competition between the radiative, bonding, and antibonding evanescent modes, which lead to attraction at all separations. Such an interplay is illustrated in Fig. 8 for the example of two gold plates. It is worth noting that, because incident light in classical systems is typically introduced over a narrow bandwidth, the scaling of gradient forces with separation is often exponential at large separations $d \gg \lambda$, where $\lambda$ is the decay length of the corresponding excited mode. In contrast, Casimir forces arise from contributions spanning many such modes, each contributing different exponential decays, the cumulative effect of which leads to the usual polynomial scaling. Hence, even if the force contributions seem to be dramatically altered within a narrow bandwidth, as is often the case in classical systems, this alteration is

---

[2] Technically $U \to \infty$ in closed PEC structures, a divergence that this is circumvented in energy calculations by exploiting renormalization procedures involving high-frequency cutoffs [5, 192]. Such cutoffs are motivated by the fact that these divergences are not physical, since real materials such as the gold plates of Fig. 8 become transparent at large $\omega$.

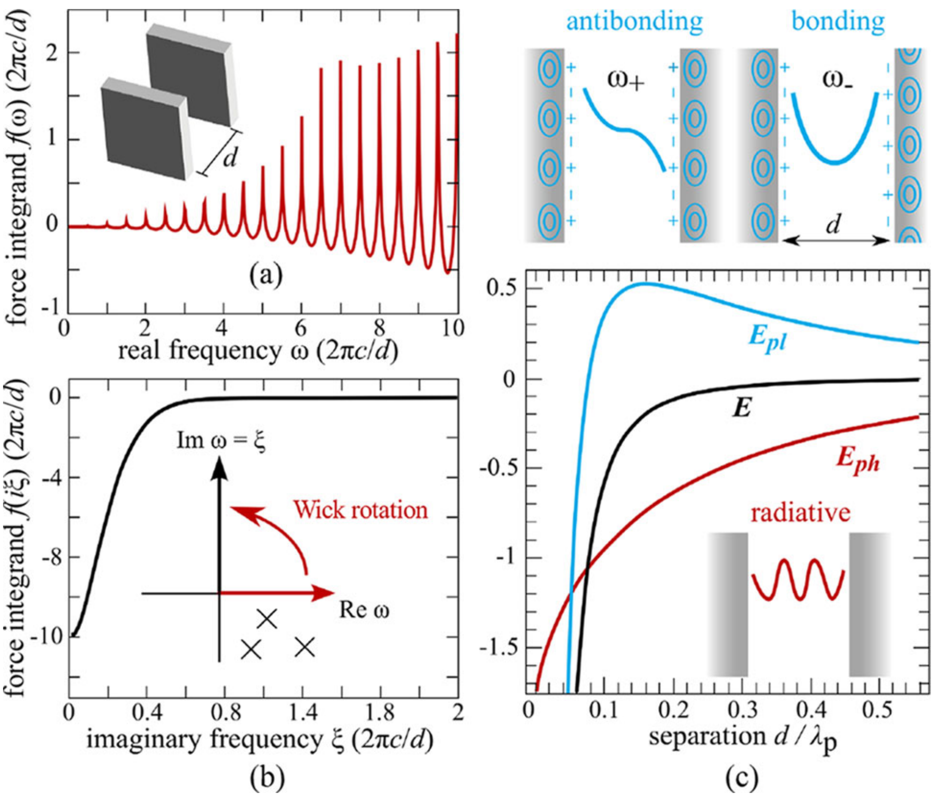

**Figure 8** Spectral decomposition of the Casimir force between gold plates illustrating the advantages of going into the imaginary-frequency axis, as well as the overall impact of propagating and evanescent modes on the force. Casimir force integrand as a function of (a) real $\omega$ and (b) imaginary $\omega \to i\xi$ frequencies, illustrating the transition from a broad-bandwidth oscillatory integrand to a smooth, exponentially decaying one (adapted from Ref. [194]). (c) Casimir energy $E$ (black line) decomposed into contributions from evanescent/plasmonic $E_{pl}$ (blue line) and propagating/photonic $E_{ph}$ (red line) modes, as a function of the plate–plate separation $d$ normalized by the plasma wavelength $\lambda_p$. The plasmonic energy switches sign from attractive in the near field ($d \ll \lambda_p$) to repulsive in the far field ($d \gg \lambda_p$), peaking at $d \approx 0.16\lambda_p$, while the radiative energy leads to attraction at all distances [201].

usually canceled by contributions at other frequencies and therefore has little influence on the force.

In addition to posing conceptual challenges, the broad and oscillatory character of the Casimir spectrum also imposes severe limitations for theoretical and numerical calculations, as reviewed in Refs. [7, 194]. The key to overcoming these problems is a well-known technique from complex analysis involving extensions of the real-frequency integrand into the complex plane, on which practically all modern calculations are based. Specifically, because the Casimir force integrand is unobservable and related to causal scattering problems (fields due to dipole antennas), it is an analytic function in the upper-half complex frequency plane ($\mathrm{Im}\,\omega > 0$), and hence the integral along real frequency is mathematically equivalent to the integral along the imaginary-frequency axis $\omega = i\xi$ [206]. Intuitively, the presence of oscillations and resonances in the Casimir integrand is linked to the fact that dipole sources oscillating at real frequencies $\omega$ produce radially propagating spherical waves $\sim \frac{\exp(i\omega r/c)}{r}$, where $r$ is the distance away from the dipole, which in turn lead to the sensitive interference and cancellation effects employed in classical designs. Along imaginary frequencies $i\xi$, however, dipole sources lead to exponentially decaying fields $\sim \frac{\exp(-\xi r/c)}{r}$, which in turn yields integrands that are smooth, non-oscillatory and exponentially decaying (decay lenghts $\propto \frac{1}{d}$) and which are highly susceptible to efficient numerical integration, e.g. numerical quadrature. The absence of resonances along imaginary frequencies extends to material responses as well, since the permittivity of passive materials $\varepsilon(i\xi)$ evaluated at imaginary frequencies decays monotonically with $\xi$ [206]. To illustrate this exponential behavior, Fig. 8(b) shows the Casimir integrand between gold plates along the imaginary frequency contour. While this imaginary-frequency perspective is crucial for numerics, it also suggests that when thinking of modifications to Casimir forces (in contrast to classical design principles that focus mainly on resonant phenomena) it is particularly useful to employ intuition from quasistatics ($\omega \to 0$), where the lack of resonances and interference effects captures the decaying, non-oscillatory physics at imaginary frequencies.[3]

## 3.2 Designer Casimir forces

Unlike classical forces, the study of Casimir forces was until recently hampered by a lack of theoretical tools. Accurate experimental measurements were also until recently extremely challenging due to the small magnitude of these interactions at large separations $\gtrsim\mu$m. The emergence of new theoretical tools and state-of-the-art experimental setups is finally enabling synergistic explorations of this phenomenon, and one emerging topic of interest is the design of structures exhibiting force behaviors that differ from the standard attractive $1/d^4$ power-law of planar PEC bodies, and which aid in reducing or altogether switching the sign of the force. As discussed below, a few of these new theoretical predictions have been realized in experiments, though the range of potential effects remains largely unstudied.

### 3.2.1 Theory

The sum-over-modes approach described above provides a conceptually useful starting point for understanding Casimir forces and has been subject to multiple modifications to include realistic structures including lossy materials and finite objects [5, 202–204, 207–210]. However, it turns out that in practice it is seldom employed for calculations, which more commonly rely on modern perspectives and theoretical techniques that lie much closer to the original picture of fluctuating dipoles introduced by van der Waals and others [178, 179]. In particular, this intuitive picture provides a direct and intuitive connection to classical scattering problems by way of the fluctuation-dissipation theorem of statistical physics [178, 206, 211], relating the dissipative properties of bodies to the resulting dipole fluctuations. Although such a relationship was first derived in the context of microscopic dipole–current fluctuations within the volumes of the bodies, more recent approaches reduce the problem to a smaller number of scattering problems involving sources and/or incident electromagnetic waves only on surfaces around bodies [7]. In fact, the first generalization of Casimir's original derivation was carried out by Lifshitz, Dzyaloshinskiĭ, and Pitaevskiĭ in the 1960s [179] where, rather than summing mode contributions, they considered instead calculations based on thermodynamic Maxwell stress tensors (ensemble average of Eq. (3)) and fluctuation–dissipation theorems of fields at equilibrium, which relate expectation values of fluctuating fields $\langle E_i E_j \rangle$ to the imaginary part of the electromagnetic Green's function (electric field due to a dipole source) [206].[4] The stress-tensor approach was originally employed as a semi-analytical method to obtain predictions in simple geometries, such as planar dielectric bodies and eventually arbitrary multilayer films [215–218].

For the next few decades, virtually all theoretical work focused on studying ways of altering the magnitude and sign of the force by employing either semi-analytical techniques or heuristic approximations involving small perturbations around known solutions, such as parallel plates [185, 219] or dilute gases [220–222]. As described in more detail in Section 3.2, approaches based on materials in planar structures relied mainly on narrow resonance effects whose contributions wash out when the full spectrum is considered [223, 224]. Modification arising from boundary effects were also studied, albeit using ad-hoc approximations valid only in the limit of small curvatures. These include pairwise additive approximations such as the well-known Derjaguin or proximity-force approximation (PFA) [217, 225, 226], which to lowest order yield the force between nearly planar bodies by summing the force per unit area of an equivalent parallel-plate geometry over all adjacent surfaces, providing an intuitive way of conceptualizing changes to the force. For instance, within PFA the zero-temperature Casimir force between a PEC sphere of radius $R$ and a PEC plate separated by distances $d \ll R$ is given by $F_C = -\frac{\hbar c \pi^3 R}{360 d^3}$ [219]. Similar closed-form expressions can be worked out for a handful of high-symmetry structures, including infinite cylinders above plates [227], in which case the force per unit length $p_C = -\sqrt{\frac{R}{2d}} \frac{\hbar c \pi^3}{384 d^3}$, with the main result being a change in the power-law of the interaction. In situations involving dilute or weakly polarizable media, approximations based on summation of van der Waals or Casimir–Polder interactions can be

---

[3] Mathematically, the exponential decay of the Casimir-force contributions at imaginary frequencies $\omega = i\xi$ tends to make the total force qualitatively similar to the $\xi = 0$ contribution, which dominate in the near-field or van der Waals regime.

[4] Note that in contrast to classical calculations, there are no ambiguities when evaluating energy or stress tensors due to fluctuations in dissipative media since in the Casimir case one is dealing with thermodynamic quantities [212–214].

employed [221, 222, 228]. Other perturbative approximations include re-normalized Casimir-Polder [229, 230] or semi-classical interactions [231], multiple scattering expansions [232–235], classical ray optics approximations [236, 237], and higher-order PFA corrections applicable to gently curved surfaces [226, 238–242].

When applied to non-planar structures with separations $d \sim$ feature sizes and in non-dilute media, these approximations fail to capture fundamental non-additive effects [9, 228] that can only be handled by more sophisticated techniques. Mirroring the development of classical electromagnetic calculations, early approaches mainly considered semi-analytical methods that expoit symmetries in specific geometries to expand the field unknowns in convenient spectral bases, such as Fourier modes or spherical multipoles [210, 220, 232, 234, 243–248]. It took almost four decades for sophisticated numerical techniques that can capture the full spectrum of non-additive effects in realistic, microstructures geometries to be developed [7, 9]. Such general-purpose methods come in a bewildering variety of flavors, including formulations based on the original stress-tensor approach, fundamentally tied to the statistics of fluctuations [206, 249], as well as more modern approaches in which the force is derived or expressed via path integrals [248, 250–254] or trace formulas involving scattering matrices [234, 245, 246, 248, 255]. Similar to classical calculations, numerical implementations vary and include spectral-basis or eigenmode expansions, e.g. Fourier series and spherical harmonics) [210, 245], or localized mesh discretizations, e.g. finite differences [249, 256–259] or boundary elements [214, 254, 260–263]. Despite their deceivingly different origins and algebraic structures, the thread connecting all of these formulations is the underlying relationship between electromagnetic fluctuations and classical scattering problems. Because many such scattering problems must be solved to compute even a single force, calculations tend to be significantly more computationally demanding than classical force simulations. However, as discussed further below, despite these complications the development of exact methods has ushered a renaissance of Casimir-force modeling in highly non-planar structures. For more in-depth discussions of theoretical methods, emphasizing the connection between classical calculations and Casimir forces, the reader is referred to Refs. [7, 194].

#### 3.2.2 Experiments

The first experimental validations of the Casimir effect date back to the 1960s, although significant sources of errors made it difficult to unambiguously confirm the existence of the force [279]. In early experiments, complications arose from the need to maintain a high degree of parallelism between plates and from the small force magnitudes present at large separations. Decades later, advances in instrumentation began making it possible to place nearby objects in close proximity with nanometer precision and slow mechanical drifts, facilitating measurements with significantly higher precisions and spatial resolutions. It wasn't until the experiments of van Blokland et al. that the force between metallic surfaces was unambiguously measured [8], followed almost two decades later with the first high-precision measurements of the Casimir force [280], ushering a new era of Casimir metrology. In order to circumvent alignment issues related to parallelism between planar surfaces, most Casimir-force measurements have since been conducted in a related geometry involving a large (tens of microns or more) sphere in close proximity to a planar body. Among the few exceptions was the experiment by Bressi et al. in 2002, which unmambiguously verified the Casimir force in the original parallel-plate geometry [281]. Readers are referred to Refs. [185, 187, 192] for a historical overview of Casimir experiments.

In most experiments, the Casimir effect manifests itself as a force that shifts the equilibrium position, or alternatively which modifies the spring constant of a compliant test body when in close proximity to a surface, similar to other distance-dependent forces like the aforementioned optical and electrostatic forces. To date, most observations rely on measuring changes in the equilibrium position of the object in question (a static effect) or force gradients (a dynamic effect) over some range of separations. Due to difficulties involving large, environmental DC noise, static measurements are less frequent than dynamic measurements of the force gradient. In what follows, we briefly describe three common sets of experimental setups, illustrated in Fig. 9, based on either torsional pendulums, dynamic-mode atomic force microscopy (AFM) or torsional MEMS oscillators.

The torsional pendulum setup developed by the Lamoreaux group, shown in Fig. 9(a), was employed in the first high-precision (5% accuracy) demonstrations of the Casimir effect and more recently in one of the first demonstrations of the thermal Casimir force [264–266]. In such an experiment, the static change due to the force exerted on two bodies (a flat, metal-coated plate and a large, metal-coated spherical lens) is directly measured in vacuum and at room temperature. While one end of the sphere is mounted on the far end of a pendulum, the other is sandwiched between two nearby compensator electrodes that enable the sphere to move.

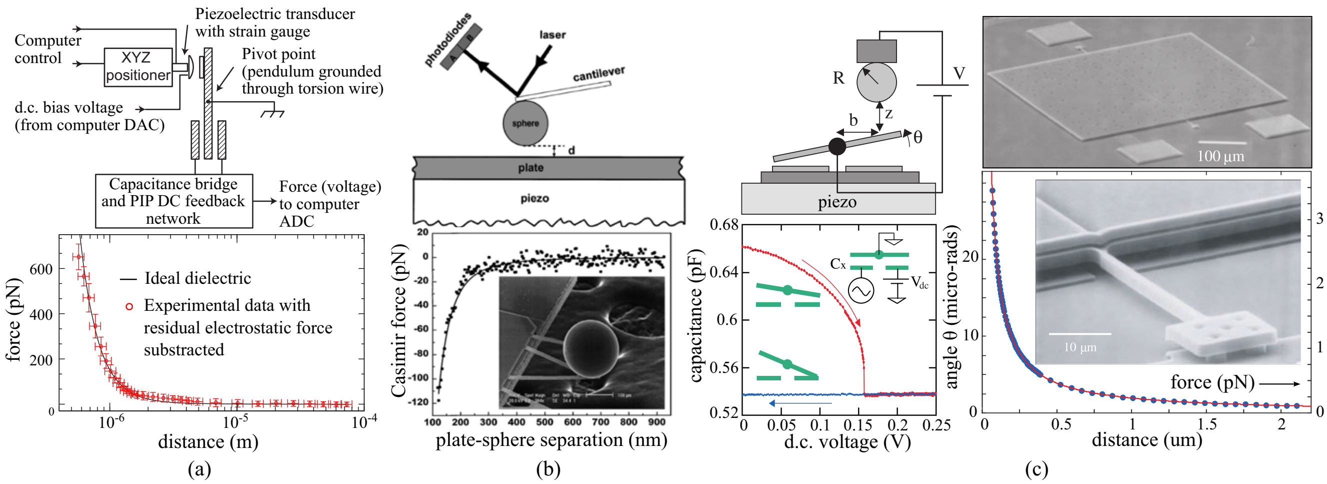

**Figure 9** Examples of various experimental setups for detecting Casimir forces, including: (a) Torsional pendulums where the static change due to the Casimir force between a sphere and a plate is measured as a change in the capacitance between two compensator electrodes. The setup and corresponding force measurements are taken from Refs. [264–266], and involve forces between a 1" gold-coated quartz plate and a gold-coated spherical lens with a radius of curvature of 11.3cm. The experimental data show the Casimir force with the residual electrostatic force subtracted from the total force measurements. (b) AFM setups where both the static and dynamic modes have been utilized for measuring the deflection and mechanical frequency-shift of a cantilever [267–277]. The experimental data is taken from Ref. [267], and shows force measurements obtained by calibrating the cantilever deflection signals. The inset illustrates the corresponding experimental apparatus, involving a metallized polystyrene sphere with a diameter of 0.2mm attached to an AFM tip. (c) Torsional MEMS oscillators driven capacitively by electrodes, where the frequency shifts due to the Casimir force can be measured electrically or optically. The setup and measurements are taken from Ref. [278], involving a doped polysilicon 500 $\mu$m × 500 $\mu$m plate anchored to a substrate and acting as a torsional oscillator. The angular displacement $\theta$ of the oscillator is obtained by measuring the capacitance change between the oscillator and the electrodes below, which involves biasing one of the electrodes and application of a small AC probing signal. The angular displacement at various sphere-plate separations is then normalized to obtain the force data.

Specifically, as these two bodies are brought closer together using a closed-loop piezoelectric transducer, the attractive Casimir force exerts a force on the sphere and a corresponding torque on the pedulum, causing an imbalance in the capacitance of the two compensator electrodes. A corresponding voltage is sent to one of the electrodes to counteract the effect of the torque and therefore restore the capacitance balance with the two electrodes, where the error signal detected and applied is directly proportional to the static magnitude of the Casimir force. With this particular apparatus, accurate measurements can often be made at separations spanning the range 0.7–7 $\mu$m.

A related scheme involves static and dynamic AFM measurements of the separation of a sphere attached to a cantilever from a surface. In the static mode, the displacement is obtained by measuring the deflection of the cantilever tip with a position-sensitive detector [267–270]. For higher detection sensitivities, both the amplitude- and frequency-modulation modes of AFMs can be used to detect the frequency shift of the cantilever. The amplitude-modulation mode works by driving the cantilever near a resonance frequency, which leads to appreciable amplitude changes in the detected signal even under small frequency shifts. Experiments adopting this measurement mode include those of Refs. [282–284]. The frequency-modulation mode of an AFM, on the other hand, offers higher sensitivity than the amplitude-modulation mode and is also more immune to amplitude noise. In this case, the cantilever is driven on resonance and the resonant frequency is monitored with a fiber interferometer and tracked with a phase-lock loop, as illustrated in Fig. 9(b). The frequency shift due to short-range attractive forces can then be obtained by frequency demodulation: it is brought close to the other test body by a closed-loop piezoactuator where the test body's position is monitored by another fiber interferometer (with sub-nm resolution). Reported achieved separations in this setup range from 200 nm to 2 $\mu$m [271–277].

Finally, the torsional MEMS oscillators employed by the Chan and Decca groups have proven useful for performing measurements at the microscopic scale [278, 285–289]. As illustrated in Fig. 9, the torsional oscillator is often a large metal or heavily doped semiconductor (e.g. polysilicon) plate suspended by thin arms and engineered to carefully tune its mechanical resonance frequency. Attached to the plate lies one of the test bodies, often a large-diameter sphere, while underneath lie two electrodes, driven by resonant and modulation signals in order to detect the capacitance change between the two, and hence the force gradient. In contrast to other setups, here calibration of the absolute separation between the test bodies can be performed by electrostatic or optical interferometric means [290].

Beyond parallelism, challenges to high precision experiments include electrostatic forces that arise due to either static potentials between different metals connecting the two surfaces, or patch potentials [291–294]. Electrostatic effects can be the dominant interaction between surfaces at large separations, and hence minmizing and accounting for their contribution is crucial for obtaining accurate measurements at $\mu$m lengthscales. In measurements where the Casimir effect reduces the mechanical spring constant of the test bodies, the typical protocol for calibrating these is by measuring the corresponding electrostatic force as a function of the applied voltage. On the other hand, patch potentials are highly sample dependent and cannot easily be altered in situ, and thus their impact is often fitted via empirical models [295–298]. These effects can become even more pronounced in polycrystalline metal films [299]. The Tang group recently developed an *in situ* scanning Kelvin probe, involving a 1mm × 1mm metallized silicon nitride membrane above an 8mm gold sphere, which enables measurements of the spatial distribution of such residual potentials, allowing in-situ detection of force gradients [294, 300] and providing a valuable technique to ascertain the role of such patch potentials on integrated, Casimir force measurements.

Mature nanofabrication and metrology techniques have begun to greatly influence force measurements, enabling careful control and calibration of material and surface properties. First, while film deposition and microfabrication of MEMS devices are straightforward, evaluating the influence of surface roughness to the Casimir effect at short distances demands care in refining the fabrication procedures against typically tolerable imperfections, including surface roughness and existence of native oxides [301–305]. The metals used in Casimir experiments are typically prepared by evaporation or sputtering in ultrahigh vacuum environment and at low deposition rates. Recent AFM measurements have been employed to survey the surface morphology, root-mean-squared (rms) roughness and peak-to-peak height variations of various metallic samples, leading to better descriptions of roughness at short lengthscales. For instance, it was found that while typical rms roughness is on the order 2 nm, peak-to-valley height variations could reach tens of nanometers. Theoretical models that incorporate such detailed descriptions of roughness are discussed in Section 3.2.3. Accurate comparison between theory and experiments also requires accurate knowledge of $\operatorname{Im}\varepsilon$ over a wide spectral region [271, 306], and variations and uncertainty among samples used in different experiments can also prove problematic. Recent efforts characterizing the dielectric spectral properties of materials under test by ellipsometry have begun to shed light on a number of these issues [307–312]. Finally, demonstrations of switchable Casimir forces with phase-change material such as $\mathrm{Ag_5In_5Sb_{60}Te_{30}}$ (AIST), which can turn from amorphous to single-crystalline state by annealing [306, 313], are paving the way for the flourishing development of versatile operations where the Casimir force can be controlled *in situ* with fast response times, and this is bound to play an impact on the accuracy of future experiments.

The recent push to measure Casimir forces in unconventional, complex geometries and the development of compatible computational tools is also beginning to encourage application of more novel fabrication techniques. Specifically, there has been growing interest in developing integrated systems for probing and even utilizing the Casimir force [290, 314, 315]. These on-chip schemes remove the need for external instrumentation needed to bring test bodies together which are often prone to mechanical drifts. In fact, microfabrication could provide a means of eliminating the experimental challenge of attaining high degree of parallelism for measurements in the plate-plate geometry [314, 316]. A particular design proposed and fabricated by the MEMS community is a silicon plate tethered by three surrounding electrostatic actuators [317], overcoming the need for direct actuation of test bodies which otherwise introduces additional spring effects into the measurement. A more recent demonstration by the Chan group employed a comb drive actuator based on a highly doped silicon-on-insulator platform that was used to indirectly introduce a movable doubly clamped beam as a force-sensing element [290], illustrated in Fig. 11(c).

#### 3.2.3 Recent developments

In the last two decades, there have been a plethora of designs and experiments aimed at modifying forces in microstructured devices, spurred for example by the potential to reduce stiction in MEMS. A commonality of

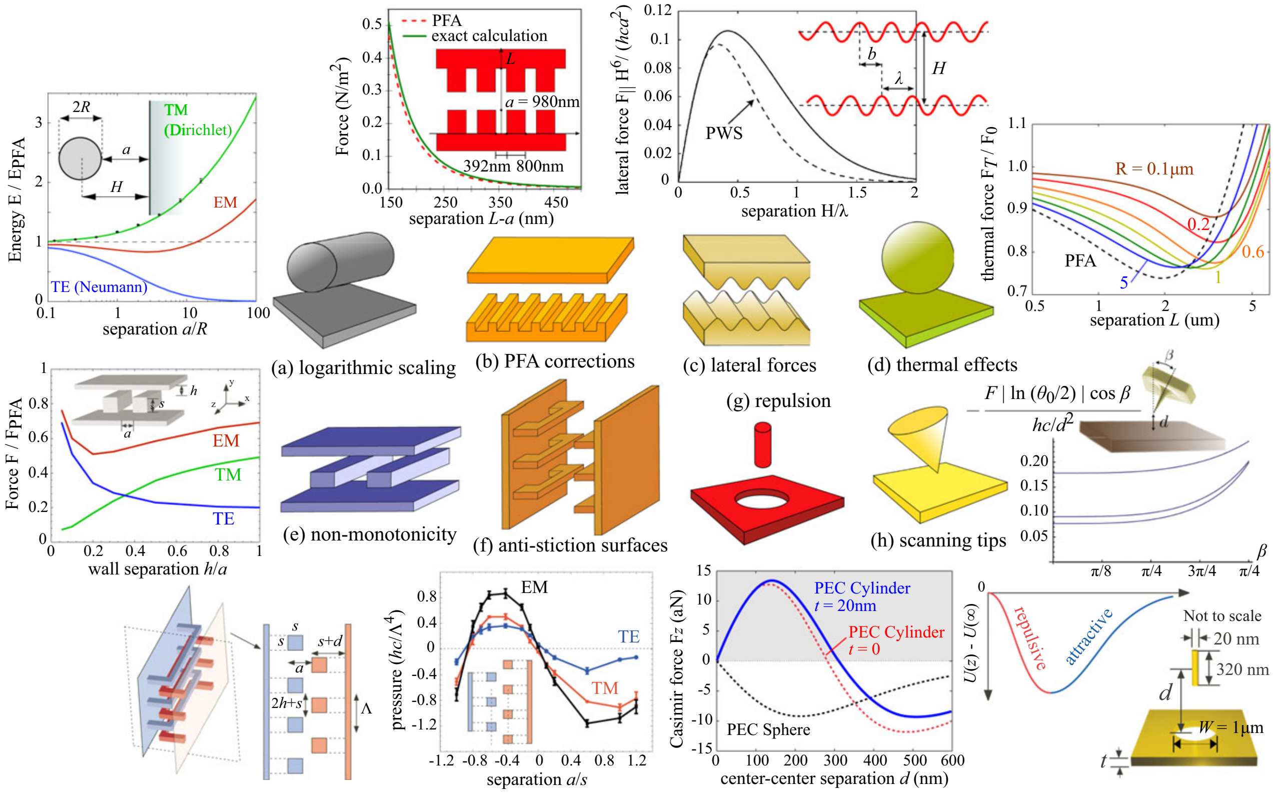

**Figure 10** Selected theoretical structures along with predictions of unusual Casimir effects. (a) Energy per unit length of a PEC cylinder of radius $R$ above a PEC plate as a function of separation $H$, normalized by the corresponding PFA energy and decomposed into both transverse-electric (TE, blue line) and transverse-magnetic (TM, red line) solutions [227]. It is found that the total force (red line) in this configuration has one of the weakest decays $\sim H^{-3}\log(R/H)$ as $H/R \to \infty$. (b) Pressure between two silicon rectangular gratings, computed by exact (green) and PFA (red) methods. (c) Normalized lateral pressure between two sinusoidally corrugated PEC surfaces of period $\lambda$ as a function of their surface–surface separation $H$, computed by both exact methods (solid) and pairwise summation (PWS) approximations (dashed) [318]. The lateral force is shown to be maximized at an optimal periodicity $\lambda \approx 2.5H$, and the PWS is shown to become progressively worse with increasing $H/\lambda \gtrsim 0.3$. (d) Thermal Casimir force $F_T$ between a gold sphere and plate at room temperature, divided by the force at zero temperature $F_0$, as a function of their separation $L$. Solid lines from top to bottom correspond to increasing values of sphere radius $R$. The dashed curve represents the same force ratio, but as computed by the PFA. (e) Force per unit length between two PEC waveguides adjacent to two PEC plates a distance $h$ apart, normalized by the corresponding PFA force and decomposed into both TE (blue line) and TM (green line) solutions [319]. It is shown that the competition and opposite behavior of TM and TE forces with respect to changes in $h$ causes the total force (red line) to have a non-monotonic dependence on $h$. (f) Pressure between two interleaved PEC zipper-like structures (with cross-section shown on the inset) involving brackets attached to plates, decomposed into both TE (blue line) and TM (red line) solutions, as a function of the center–center separation $a$ between the brackets [320]. The competition between lateral and normal forces leads to a change in the sign of the force, becoming repulsive at an intermediate separation due to lateral attraction between the brackets. (g) Casimir force between a small cylindrical particle and a plate with a hole of size $W$ as a function of their center–center separation $d$, for both gold (blue) and perfect metal (dashed red) material configurations [321]. The force becomes repulsive at small separations $d \lesssim W/3$, which is explained from the fact that (by symmetry) the energy of a small $z$-oriented dipole located at the center of an infinitesimally thin plate with a hole is equal to the energy of an equivalent, isolated dipole. (h) Thermal Casimir force between a tilted PEC cone suspended above a PEC plate by a distance of $1\ \mu$m, as a function of the tilt angle $\beta$, for multiple temperatures $T = 300, 80$, and $0K$ (top to bottom).

current efforts is the search for structures that exhibit strong deviations from the additivity inherent in pairwise approximations such as PFA. Other efforts focus on discovery of structures/materials exhibiting strong material/temperature effects. Recent predictions include strong interplay between geometry and temperature effects in sphere–plate geometries, lateral forces between corrugated plates, non-monotonic forces between

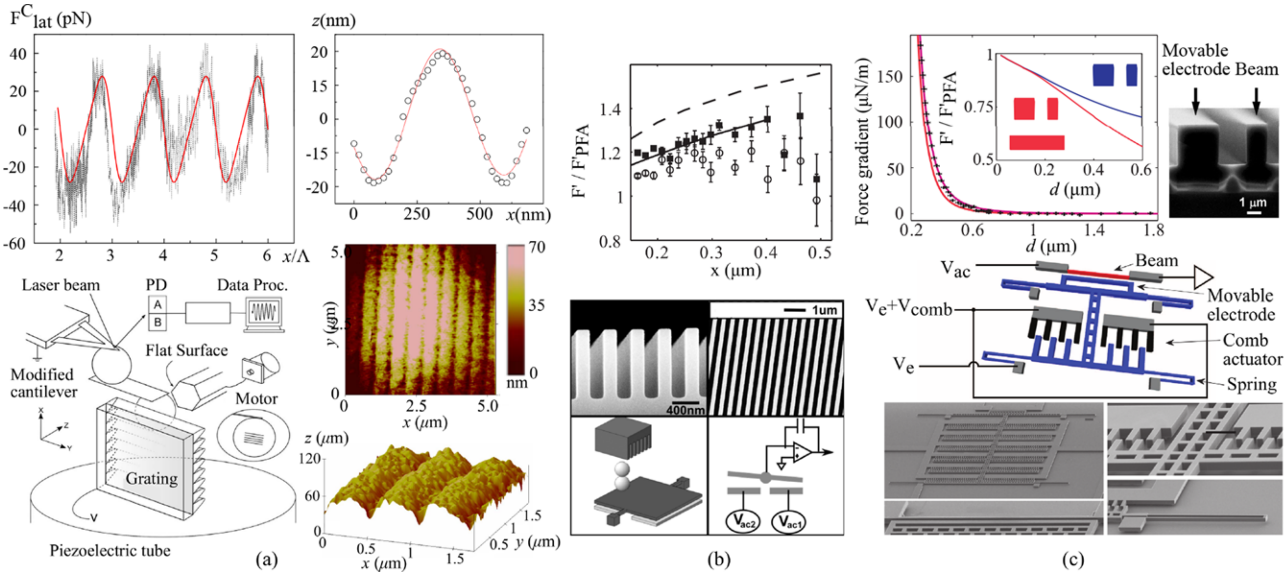

**Figure 11** Recent experimental demonstrations of lateral forces, deviations from PFA, and finite-size effects in microstructured geometries. (a) Schematic of experimental setup used to measure lateral Casimir forces (i), involving an AFM system comprising two test bodies, a polystyrene sphere of diameter 200 $\mu$m and a plate, whose surfaces are covered with longitudinal corrugations of average period $\Lambda \approx 574.7$ nm [341]. Also shown are AFM scans (ii,iii) of the corrugated surface of the sphere along with a cross-section (iv) of the grating surface, where the solid line shows a sine function obtained by fitting. The plot (v) shows the measured lateral force (black dots) as a function of lateral displacement $x$ for a single separation of $124.7$ nm, whose asymmetric pattern shows good quantitative agreement with exact theoretical predictions (red line). (b) Lateral (i) and top (ii) cross-sections of a rectangular trench structure with periodicity $\Lambda = 400$ nm and depth $t = 0.98$ $\mu$m, suspended above two stacked silica spheres of diameter $50$ $\mu$m mounted on a movable silicon plate (iii,iv). Plotted is the ratio $F'/F'_{PFA}$ of the measured Casimir force gradient between the top sphere and the grating, normalized by the corresponding PFA force gradient, as a function of their surface–surface separation $d$, for samples with $2\Lambda/t = 1.87$ (circles) and $2\Lambda/t = 0.82$ (squares). Also plotted are theoretical predictions based on exact methods [247], which demonstrate strong deviations from PFA. (c) Schematic of an integrated experimental setup (i) along with corresponding scanning-electronic micrographs (ii,iii) of a structure involving a silicon beam (red) and a movable silicon electrode and comb actuator supported by four springs (blue), with electrical connections [290]. The plot (iv) shows the measured Casimir force gradient between the beam and electrode (black dots) as a function of separation $d$, along with exact theoretical calculations in the absence (red line) and presence (purple line) of electrostatic patch potentials. The inset shows the calculated force normalized by the expected PFA force in the presence (red) and absence (blue) of the substrate, showing that multi-body effects become appreciable at separations $d \gtrsim 2$ $\mu$m.

waveguides, reduced forces between rough surfaces, and even repulsive forces arising from geometry alone. A selection of representative structures and predictions of unusual behaviors are shown in Fig. 10. Figures 11 and 12 describe recent experiments exploring force modifications based on either geometrical or materials approaches.

The first investigations of non-additive or unusual geometric effects considered idealized situations that proved to be theoretically convenient but experimentally unrealistic. These include predictions of repulsive or expansive self-forces in hollow PEC and exotic-dielectric shells [185, 322–324] or "Casimir pistons" consisting of two PEC blocks sliding between PEC walls [325–327], which later proved problematic. For instance, the repulsive effect was shown to disappear if the sphere is cut in half [328] and also goes away when realistic materials are considered in which case the Casimir energy is highly dependent on artificial, high-frequency cutoffs [192, 329, 330]. Repulsive forces on PEC boxes were also invalidated when the box expansions were replaced by the rigid motion of a "piston" sliding through a wall [326]. A second wave of predictions and experiments considered more realistic structures, starting with the convenient sphere–plate configuration.

Despite the commonality of sphere– and cylinder–plate geometries in experiments, exact predictions in these systems were obtained only recently. A state of the art calculation in 2006 was a semi-analytical calculation by Emig. et al. in which the force between an infinite PEC cylinder above a PEC plate was computed via path integral techniques [227]. The results, shown

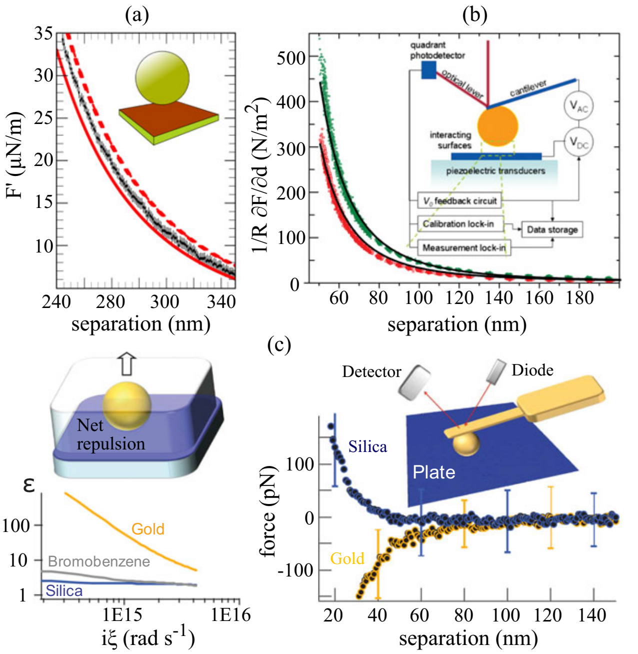

**Figure 12** Recent experimental demonstrations of modifications to Casimir forces due to material effects (all involving AFM setups). (a) Measured force gradient between a silica sphere of radius 54 $\mu$m, coated with 280 nm gold film and suspended above a graphene-coated silicon-on-insulator substrate (black crosses), along with corresponding predictions from the Lifshitz theory in the absence (solid line) and presence (dashed line) of the graphene sheet [277]. The graphene sheet is shown to increase the Casimir force by $\approx 10\%$. (b) Measured gradient force between a gold-coated polystyrene sphere of radius $R = 100$ $\mu$m and gold thickness $\sim$100 nm and either a gold-coated (green square) or ITO-coated (red squares) silica plate, as a function of their surface–surface separation $d$ [282]. The black lines indicate calculated Casimir forces with the addition of residual electrostatic forces. The use of oxides is shown to halve the Casimir force by roughly 50%. (c) Measured attractive (orange) and repulsive (blue) Casimir forces between a gold sphere and either a silica or gold plate, respectively, immersed in bromobenzene [346]. Also plotted are the dielectric permittivities $\varepsilon$ of gold (orange), bromobenzene (gray), and silica (blue) evaluated at imaginary frequencies $i\xi$, whose dielectric arrangement over a wide range of $\xi$ leads to repulsion [179].

in Fig. 10(a), demonstrated an unexpectedly weak, logarithmic decay $\sim d^{-3}\log(R/d)$ at large cylinder–plate separations and provided the first exact prediction of finite temperature contributions (beyond quantum fluctuations) in an open geometry. Ironically, it took a few years for the sphere–plate geometry to be explored by exact methods [331–333], demonstrating departures from PFA at unexpectedly short separations. Variations of these structures to include interacting (even eccentric) cylinders, spheres and ellipsoidal bodies, would eventually be studied as well [244, 245, 332, 334–337]. An interesting geothermal effect involving nontrivial interplay between geometry and temperature was recently predicted in the sphere–plate geometry, wherein thermal fluctuations on the scale of the thermal wavelength lead to strong departures from PFA and even nonmonotonic behaviors Fig. 10(d) below certain critical temperatures [332, 338, 339]. The interaction between sharp-shaped conductors, such as wedges and cones or the tip of a scanning tunneling probe, and planar substrates was also recently explored, as seen in Fig. 10(h), and shown to also exhibit significant temperature corrections [340]. No experiments have yet probed these geometric effects.

Calculations and experiments demonstrating nonadditive effects in extended geometries include sinusoidal corrugated and grating structures, starting with the early experiments of Roy et al. [342]. Perturbative expansions in the separation and corrugation depth of the structures proved useful as they lead to constraints on the range of validity of PFA in these systems, but soon had to be extended to capture wavelength-scale features. Ref. [343] considered PEC gratings beyond PFA by employing path-integral and scattering matrix techniques, demonstrating $\sim$20% deviations from PFA predictions in structures with periods $\lambda \sim$ separations. A recent experiment by Chan et al. measured forces in a similar, albeit realistic structure consisting of a gold sphere above a silicon nanoscale rectangular grating, illustrated in Fig. 11(b) [288], which was subsequently followed up by theoretical calculations, also shown in Fig. 10(b), accounting for changes from the finite permittivities of the materials [247]. Comparison of the experimental measurements with the PEC predictions of Ref. [343] are shown in Fig. 11(b) along with the experimental setup, which consisted of force-gradient measurements obtained via shifts in the oscillation frequency of the torsional oscillator on which the sphere was mounted. Fig. 10(b) shows the theoretical predictions by Guerout et al. which include material effects and confirm deviations from PFA on the order of 10–20%. Extension of these studies which consider different grating profiles, lengthscales, and even 2d-periodic structures have been explored [210, 344, 345], demonstrating strong interplay between geometry, material, and temperature effects; there are even recent claims of dramatic force reductions (on the order of 80%) in gratings with sub-100 nm features [289], although the source of such a reduction has yet to be clearly identified.

In addition to normal forces, it is also possible to engineer lateral Casimir forces that act tangentially to the interacting surfaces, e.g. by breaking translational symmetry. The lateral force between sinusoidal corrugated surfaces was among the first realistic structures to be studied using exact methods [251, 347, 348], leading to predictions of optimal modulation lengths for which lateral forces are maximized, as shown in Fig. 10(c). Applications of lateral forces to noise-driven ratchets [349] and non-contact pinions [350] were subsequently explored due to their potential impact on MEMS. The first experimental demonstration of such a lateral force was performed in 2002 by Chen et al. using an AFM setup comprising a sphere adjacent to a flat plate with nanoscale sinusoidal corrugations of amplitudes $\sim$5–60 nm and periods $\lambda \approx 1.2\ \mu$m much larger than the separation between the bodies. Figure 11(a) shows measurements and a schematic of a similar setup from a more recent experiment [341] based on structures with smaller periods, $\lambda \approx 0.5\ \mu$m, and larger corrugation depths, in which larger deviations from PFA and asymmetric dependencies on the lateral displacement between the plates were observed. Using a related setup, the same authors measured the dependence of the force as a function of the angle between the corrugations [270]. A related structure consisting of Ni-corrugated surfaces, one of which is hidden under a thin metallic film, has also attracted recent interest [351] due to predictions of strong variations in the normal force with the lateral positions of the surfaces and its corresponding sharp dependence on the choice of metal. Such a system would allow unambiguous investigations of the role of dissipation on the thermal Casimir force, a subject of recent controversy [184, 187, 351].

Progress in modeling nanostructured surfaces has also led to significant breakthroughs in understanding the role of surface roughness (disordered surfaces) on measurements at nanometric separations. In this regime, roughness and gap distances are on the same scale thereby obscuring the corresponding distance upon contact between surfaces (or absolute measurements of the separations) [353]. While predictions based on perturbative approximations such as PFA played a key role in early experiments [302, 354–357], the push to explore Casimir forces at shorter separations has motivated more nuanced and precise theoretical studies of roughness [303, 304, 358]. For instance, recent Casimir-force measurement in the sphere–plate geometry demonstrated that at separations $\lesssim$100 nm, roughness effects manifest as strong deviations in the power-law scaling of the force, leading to large discrepancies $\sim$100% between exact and perturbative theoretical predictions [303]. Recent works have also explored the strong interplay between surface-roughness modulation and curvature, demonstrating significant modifications to the force power-law depending on the roughness profile [359]. Application of brute-force techniques [258, 259] has made it possible to perform reliable statistical studies of roughness effects on the force at separations comparable to the root-mean square of the height fluctuations, where the impact of shape, size, and contribution of spurious peaks or asperities is non-negligible [304].

The failure of PFA is even more pronounced in complicated, multi-body geometries, such as the structure shown in Fig. 10(e), involving two metallic co-planar waveguides suspended above adjacent metal plates. Using brute-force numerics, Ref. [319] found that the attractive Casimir force per unit length between the waveguides varies non-monotonically as a function of their separation from the plates, decreasing and then increasing as the plate separation decreases from infinity to zero. It was found that the force deviates from PFA by approximately 40% in the limit of two isolated waveguides ($d \to \infty$) and is largest when the adjacent plates come into contact with the waveguides, in which case the structure approaches the Casimir "piston-like" geometry studied previously by analytical means [325]. More interestingly, application of simple pairwise, line-of-sight approximations like PFA in which one sums the lateral-force contribution of the plates to the waveguides, predicts a monotonically increasing force with increasing plate separation [360]. Extensions of this structure to cylindrical waveguides [334, 361] and exotic materials [259] have been explored, along with explanations of the non-monotonicity which arises from non-additive, screening effects [334]. A recent experiment by Chan et al. measured force gradients in a related geometry via the novel, integrated setup described in Section 3.2.2, involving a silicon beam and an electrode suspended above a silicon plate, whose cross-section is shown Fig. 11(c) [290]. Although a significant step in the right direction, the experiment was performed at length-scales and separations that precluded significant multi-body effects from being observed.

Aside from non-monotonicity, one might ask whether it is possible to significantly reduce or even flip the sign of the force from attractive to repulsive. Design principles for achieving repulsion have eluded theorists and experimentalists for decades, and currently there are only a handful of ways of doing so. Materials approaches date back to the early days of Lifshitz's theory and commonly involve fluids [6, 179, 199, 254, 362, 362–364] and/or exotic materials [365–369]. In fact, the influence of repulsive Casimir forces on fluid suspensions and on wetting phenomena in thin films [189] motivated much of the foundational work of Lifshitz, Dzyaloshinskiĭ, and Pitaevskiĭ [179], and has since played a crucial role in colloidal physics and microfluidics [6, 189, 370]. Repulsion can arise for instance in situations involving dissimilar bodies immersed in fluids, a phenomenon that was first predicted in the van der Waals regime of near-field dipolar interactions. Specifically, the van der Waals force between two fluctuating dipoles of different polarizabilities can flip sign, becoming repulsive when immersed in a fluid of intermediate polarizability. Generalizations of this fluid effect to situations involving macroscopic bodies and retardation were performed in the 1960s [179] but only recently observed in experiments [346]. As illustrated in Fig. 12(c), measurements by Munday et al. reveal that the long-range Casimir force between a gold-coated sphere and a silicon plate immersed in bromobenzene is repulsive; in contrast, the force becomes attractive when the plate is replaced by a thick gold film. Because such repulsions depend on the dielectric properties of materials over a wide range of wavelengths, not all fluid–material combinations lead to repulsion. Current experimental efforts are shedding light on these issues by developing tighter bounds on material properties of common fluids and by exploring broader sets of material configurations [309, 310]. Recent theoretical works have also focused on ways of exploiting material dispersion in addition to nanostructuring to obtain stable fluid suspensions and large temperature corrections [363, 371–375].

It has proven significantly more challenging to procure unusual effects in vacuum-separated structures, especially in the original geometry of two semi-infinite half-spaces where the only degrees of freedom are the choice of materials. Early attempts to obtain repulsion focused primarily on exotic materials such as perfect magnetic conductors [365], and more recently gain media [366] as well as topological [376] and Chern [369] insulators.[5] One trend in the past few years has been to study “metamaterials” formed from metals and dielectrics arranged into complex microstructures with sub-wavelength (nanometric) features that lead to exotic effects at infrared wavelengths. Examples include effective magnetodielectric, chiral and paramagnetic metamaterials that were initially predicted to strongly alter Casimir interactions [367, 368, 378, 379]. Unfortunately, while metamaterials have proven useful in classical-force designs (as described above), they often rely on narrow-band resonances that turn out to have a negligible effect on the force once the full spectrum and realistic microstructures are considered [223, 224, 380]. In fact, general arguments based on the passivity of dielectric (non-magnetic) materials discount the possibility of repulsion in general multilayer systems [381]. There is also growing interest in understanding the influence of magnetism on the force in realistic materials. For instance, Ref. [382] recently showed that magnetic effects in common diamagnetic and paramagnetic materials have little to no impact on the force, in contrast to ferromagnetic materials such as Co and Fe that can potentially enable temperature-tunable interactions if one operates near their phase transition temperature [382]. Follow-up experiments with Ni-coated surfaces operating near room temperature have demonstrated small changes to the force [276]. Finally, reductions in the force can also be achieved by modifying material properties at the atomic/electronic level, such as by varying the doping [383, 384] or carrier [385] densities of semiconductors like silicon, or by employing aereogels with varying porosity [386].

Structural approaches have only recently begun to be explored, thanks largely to the emergence of powerful theoretical techniques. These sophisticated formulations have also been used to establish general limits on the kinds of repulsive interactions that can arise through structural considerations alone. For instance, one can show that the force between multilayer films [381] or mirror-symmetric objects [387] separated by vacuum is always attractive, and also that stable suspensions (local equilibria) between vacuum-separated metal/dielectric objects are impossible [388]. There remain however many other circumstances of interest. In planar systems the only structural degrees of freedom are the thicknesses of films, which can be varied to obtain non-negligible reductions in the force [383, 389]. For instance, decreasing the thickness of a metal film beyond its corresponding bulk skin-depth in the infrared to ultraviolet regime, i.e. $\lesssim 10$ nm for common metals, causes the film to become increasingly transparent (non-reflective) and this results in a corresponding decrease in the Casimir force. The first observations of the skin-depth effects were performed by Lisanti et al. in 2005 by employing an AFM setup involving a metal-coated polystyrene sphere positioned above a micromachined torsional oscillator [390, 391]. A reduction in the Casimir force on the order of 30% was obtained with thin $\sim 0.1$ nm films, in agreement with theoretical predictions based on the Lifshitz theory. Another experiment Fig. 12(b) measuring forces between a 100 $\mu$m gold-coated sphere and gold-coated silica plate in the 50–150 nm separation range demonstrated a 50% reduction in the Casimir force

---

[5] Application of the Lifshitz theory to non-passive materials like gain media requires care, since such media violate fundamental assumptions of thermodynamic equilibrium [377].

when switching from gold to indium tin oxides (ITO) coatings due to the latter's significantly smaller plasma frequency [282]. Other efforts include investigations of forces between graphene sheets [392], whose unique mechanical, electrical, and optical properties are proving useful in a wide range of applications. For instance, the experiment of Banishev et al. recently showed Fig. 12(a) that depositing a graphene sheet on a silicon/silica substrate can increases the force by $\sim$10% [277].

Predictions of repulsion in highly non-planar systems have also emerged in the past few years. For instance, two interleaved objects such as the zipper-like glide-symmetric structure shown in Fig. 10(f) involving interleaved metal brackets attached to parallel plates, can repel one another due to a competition between lateral and normal forces. In particular, depending on the separation, the attractive lateral force between the brackets can dominate the interaction and either contribute toward or act against the attractive plate–plate and plate–bracket interactions, the net result of which is attraction at large and short separations and repulsion at intermediate separations. Although such an effect can be qualitatively understood from pairwise interactions, it was recently confirmed by exact calculations that also illustrate the dramatic, quantitative failure of PFA in highly non-planar structures [320]. Experimental demonstrations of this effect are currently being pursued by H. Chan and collaborators. A more direct and less ambiguous prediction of geometry-induced repulsion (in non-interleaved geometries) was recently made by Levin et. al., demonstrating that the force on a small elongated object centered above a plate with a hole switches from attractive to repulsive as the object approaches the plate Fig. 10(g). This effect was explained via a symmetry argument in an idealized geometry involving an infinitesimal particle or dipole above an infinitesimally thin perfect-metal plate with a hole, and validated via brute-force calculations in realistic geometries and materials. Although this was the first demonstration of a geometry-based repulsive effect that cannot arise from pairwise attractions, the magnitude of the force is unfortunately too small for current experimental detection and other alternatives are currently being explored [393, 394].

Finally, in addition to normal and lateral forces, quantum fluctuations can also induced torques on objects that are free to rotate. For example, torques can arise in anisotropic or birefringent materials [395–399] or through geometry [255, 400–402]. To date, however, there have been no experimental observations of such QED torques.

### 3.3 Technological impact

The unavoidable impact of Casimir forces on MEMS has been a driving force behind much of the recent progress discussed above, especially as scaling issues and additional complexity continue to push devices toward increasingly smaller (nanometric) scales. The adhesion or stiction of neighboring movable parts in micromachines from electrostatic or Casimir forces is of special concern, as described in a number of seminal works [173, 174, 353]. On the other hand, the ability to tune Casimir forces in MEMS can potentially lead to novel functionalities and architectures. Examples include driven nonlinear electromechanical oscillators [278, 285, 403], rack pinions based on lateral forces [404], and ultra-sensitive sensors based on parametric amplifiers [405]. Recent theoretical predictions even suggest that roughness can have a potentially positive influence on the actuation dynamics of MEMS at nanometric scales [358]. The experiment by Chan et al. in 2001 demonstrated that at short separations, the Casimir interaction between a metal sphere attached to a movable oscillator and a plate adds a nonlinear term to the otherwise linear mechanical restoring force on the sphere, resulting in a number of interesting nonlinear dynamical effects such as bistability and hysteresis [278, 285]. Meanwhile, experiments such as those by Zhou et al. demonstrating in-situ measurements of Casimir forces in on-chip integrated silicon devices continue to bring Casimir forces into the forefront of MEMS technology [290]. Anti-stiction mechanisms based on lateral forces [320] in similar integrated platforms are currently being explored.

The integration of Casimir forces and optomechanical devices offers even more degrees of freedom for achieving designable actuation effects in new generations of NOEMS. For instance, repulsive optical forces can be used to combat stiction, bringing to bear the unique competitive edge of gradient-force designs in optomechanical systems [314, 315]. The interplay and expression of Casimir and gradient forces were recently studied in systems based on coupled waveguides [315] and PhC membranes [314]. Simulations reveal Fig. 13 that all-optical, anti-bonding forces excited by incident light at relatively low powers ($\lesssim$10 mW) can be used to control the onset of stiction at small separations ($\lesssim$100 nm), and can also greatly influence the static and dynamical mechanical state of these systems [314]. The large interaction areas of PhC membranes not only allow strong Casimir effects to arise at larger separations, relaxing the signal-to-noise requirements for accurate detection, but also provide a mechanism for the simultaneous actuation and detection of Casimir forces.

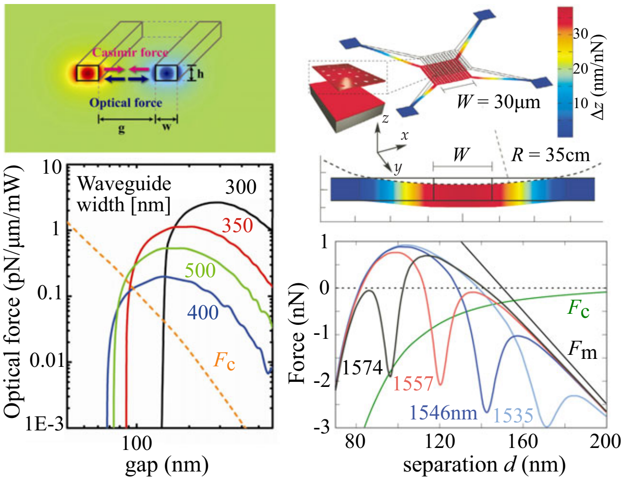

(a) (b)

**Figure 13** Theoretical investigations of the interplay between Casimir and optical gradient forces in two representative optomechanical structures (shown schematically) [314, 315]. (a) Optical (solid lines) and Casimir (dashed line) force per unit length and per mW of incident power between two rectangular silicon waveguides of height 220 nm, plotted for multiple configurations of waveguide widths. Because the Casimir force increases more rapidly than the optical force, increasingly larger powers are required to counteract stiction in this system. (b) Total force (solid lines) on a 30 $\mu\mathrm{m} \times 30\ \mu\mathrm{m}$ PhC square membrane of 130 nm thickness suspended above a silicon-on-insulator substrate by four deformable arms, as a function their surface–surface separation $d$. The total force includes mechanical (dashed black), Casimir (dashed green) and anti-bonding gradient forces. The optical force is induced by normally incident light from above with power $P = 10$ mW and (variable) wavelength $\lambda$. The stable position of the membrane varies depending on the incident wavelength, displaying bistability as $\lambda$ is swept from smaller to larger values. The schematic shows that most of the deformation occurs within the $L = 30\ \mu$m arms supporting the membrane.

Initial experiments in a related structure Fig. 6(b) demonstrate nanometer-range pulling ($\sim$1 nm/1 mW) and optomechanically induced optically bistability effects [89, 134]. By combining the above ingredients, the prospect of real-time monitoring and control of MEMS/NEMS through optomechanical degrees of freedom is becoming increasingly possible.

## 4 Concluding remarks

Because of the infinite variety of possible geometries, and the highly nonlinear dependence of electromagnetic fields and forces on the geometric and material parameters, it is impossible to be certain what the future holds for optomechanical interactions in nanophotonics. This is, perhaps, especially true for fluctuation-induced interactions, where both theory and experiment have only just begun to move past the simplest planar structures of the past. The combination of optomechanical interactions with other phenomena, such as nonlinear optics (including nonlinear-gain media and lasers), exotic plasmonic metamaterials, or fluid-mechanical effects, has been only lightly explored at best. One possible avenue for such explorations, which has been gaining ground in other areas of photonic design but is thus far little-used in the regime of classical and quantum forces, is computational "inverse design" in which hundreds or thousands of parameters are explored systematically by optimization techniques in order to discover new geometries and new regimes of operation [406].

**Key words.** Fluctuations, Optomechanics, Casimir effect, Optical forces, Gradient forces, Bonding, Antibonding, MEMS, Photothermal forces.

**Alejandro Rodriguez** is an Assistant Professor of Electrical Engineering at Princeton University, working in the areas of fluctuation-induced interactions and nanophotonics. He received B.Sc. and PhD degrees in Physics from MIT in 2003 and 2006, respectively, and was a Postdoctoral Fellow at Harvard University from 2010–2013. He has co-authored over 50 publications and holds four patents in fields such as nonlinear nanophotonics, Casimir and optomechanical forces, and radiative heat transport, and also helped co-develop one of the first numerical methods for computing Casimir forces and non-equilibrium radiative heat transfer between micro-structured bodies. Prof. Rodriguez was the recipient of the 2011 Department of Energy Fredrick Howes Award in Computational Science and was also recently named a World Economic Forum Global Shaper.

**Pui-Chuen "Wallace" Hui** received his doctoral degree in Engineering Sciences from Harvard University in 2014. His PhD work in the Laboratory of Nanoscale Optics of Prof. Marko Lončar focuses on the detection and optomechanical counteraction of the Casimir effect in integrated micro-optoelectromechanical systems (MOEMS), as well as nonlinear optomechanics. Dr. Hui received an SM in Engineering Science from Harvard University in 2012. He obtained his BS in Applied and Engineering Physics from Cornell University in 2008, where he worked with Prof. Farhan Rana on terahertz biomolecule detection and Prof. Alex Gaeta on nonlinear optics. He is a recent recipient of the Croucher Fellowship for postdoctoral research.

**Dr. David Woolf** received a B.S. degree with High Honors in Optical Science and Engineering from University of California, Davis in 2005. While earning his degree, the NSF-supported Center for Biophotonics Science and Technology (CBST) Student Fellowship gave him the opportunity to work part time under Prof. Atul Parikh on biologically active photonic crystal sensors beginning in 2003. In 2013, Dr. Woolf received his PhD in Applied Physics from Harvard University, under the supervision of Prof. Federico Capasso. His work on optomechanical devices led to the demonstration of the largest ever repulsive optical, anti-bonding force between a suspended photonic crystal membrane and a substrate. Dr. Woolf is currently employed at Physical Sciences, Inc and is working on various topics involving photonics, plasmonics, and metamaterials.

**Steven G. Johnson** is Associate Professor of Applied Mathematics at MIT, where he joined the faculty in 2004. He received his PhD in physics in 2001 from MIT, where also received three bachelor's degrees in 1995 (in physics, math, and computer science). He is author or co-author of over 150 journal articles and 27 issued patents, mostly on the design and understanding of nanophotonic systems and photonic crystals, in which wavelength-scale structures are used to modify the behavior of light, as well as a 2008 textbook on photonic crystals. He is also known for several free/open-source numerical software packages, including the MPB and Meep electromagnetic modeling tools, and also the FFTW package for fast Fourier transforms (for which he received the 1999 Wilkinson Prize for Numerical Software).

**Marko Lončar** is the Tiantsai Lin Professor of Electrical Engineering at Harvard' University's School of Engineering and Applied Sciences. He received his Diploma (1997) from the University of Belgrade (Republic of Serbia) and his MS (1998) and PhD (2003) degrees from California Institute of Technology, all in electrical engineering. Prof. Lončar's research focuses on phenomena resulting from the interaction of light and matter on a nano-scale level. He has made contributions to the fabrication, understanding, and application of optical nanocavities, diamond nanophotonics, quantum optics, nanoscale optomechanics, and cavity-based bio-chemical sensing. He is interested in the development of functional nanophotonic devices, and their integration into systems that can be used for optical communication and optical signal processing, life sciences and quantum optics. He is the recipient of an NSF CAREER Award in 2009, and an Alfred P. Sloan Fellowship in 2010.

**Federico Capasso** is the Robert L. Wallace Professor of Applied Physics and Vinton Hayes Senior Research Fellow in Electrical Engineering at Harvard University. He received a Doctor of Physics degree (summa cum laude), from the University of Rome, Italy, in 1973. After doing research in fiber optics at Fondazione Bordoni in Rome, he joined Bell Laboratory in 1976. In 1984, he was made a Distinguished Member of Technical Staff and in 1997 a Bell Labs Fellow. At Bell Labs, he held the posts of Head of the Quantum Phenomena and Device Research Department and the Semiconductor Physics Research Department between 1987 and 2000. From 2000 to 2002 he was Vice President of Physical Research at Lucent Technology. In 2003, Capasso left Bell to take up a faculty position at Harvard University. In collaboration with a wide range of multi-disciplinary scientists and engineers, he has made a series of very important contributions to solid-state physics, devices, materials, and applications, including the development of low-noise quantum-well avalanche photodiodes, resonant tunneling transistors, new memory devices and the quantum cascade laser (QCL). Capasso's current research is focused on engineered surfaces that can be used to make flat optical components by phase control on a surface. Prof. Capasso is a Fellow of the American Academy of Arts and Sciences, the Institute of Physics (UK), the American Association for the Advancement of Science, the International Society for Optical Engineering (SPIE), the Optical Society of America, the IEEE and the American Physical Society. He holds four honorary doctorates, and received numerous awards including the 2011 Galileo Galilei Medal of the Italian Society for Optics and Photonics, the 2011 Jan Czochralski Award of the European Materials Research Society, the 2010 Julius Springer Prize in Applied Physics, the 2010 Berthold Leibinger Zukunfts Preis (Future prize), and many others.

## References

[1] E. F. Nichols and G. F. Hull, Astrophys. J. **17**(5), 315–351 (1903).
[2] J. D. Jackson, Classical Electrodynamics, third edition (Wiley, New York, 1998).
[3] A. Ashkin, J. M. Dziedzic, J. E. Bjorkholm, and S. Chu, Opt. Lett. **11**(5), 288–290 (1986).
[4] Z. M. Zhang, Nano/Microscale Heat Transfer (McGraw-Hill, New York, 2007).
[5] P. W. Milonni, The Quantum Vacuum: An Introduction to Quantum Electrodynamics (Academic Press, San Diego, 1993).
[6] J. N. Israelachvili, Intermolecular and Surface Forces (Academic Press, London, 1991).
[7] S. G. Johnson, Numerical methods for computing casimir interactions, in: Casimir Physics, edited by D. A. R. Dalvit, P. Milonni, D. Roberts, and F. D. Rosa, Lecture Notes in Physics Vol. 836 (Springer–Verlag, 2011), chap. 6, pp. 175–218.
[8] P. H. G. M. van Blokland and J. T. G. Overbeek, J. Chem. Soc. Far. Trans. I **74**, 2637–2651 (1978).
[9] A. W. Rodriguez, F. Capasso, and S. G. Johnson, Nat. Phot. **5**, 211–221 (2011).
[10] P. Lebedew, Annalen Der Physik **6**(11), 433–458 (1901).
[11] E. F. Nichols and G. F. Hull, Phy. Rev. **17**(2), 91–104 (1903).
[12] Y. I. Salamin and C. H. Keitel, Phys. Rev. Lett. **88**, 095005 (2002).
[13] S. Chu, Science **253**(5022), 861–866 (1991).
[14] D. G. Grier, Nature **424**, 810–816 (2003).
[15] K. Dholakia, Nat. Mater. **4**, 579–580 (2005).
[16] S. Chu, J. E. Bjorkholm, A. Ashkin, and A. Cable, Phy. Rev. Lett. **57**(3), 314–317 (1986).
[17] S. Chu and C. Wieman, J. Opt. Soc. Amer. B-Opt. Phy. **6**(11), 2020–2020 (1989).
[18] P. D. Lett, W. D. Phillips, S. L. Rolston, C. E. Tanner, R. N. Watts, and C. I. Westbrook, J. Opt. Soc. Amer. B-Opt. Phy. **6**(11), 2084–2107 (1989).
[19] Laser-cooled and trapped atoms (Pergamon, New York, 1984).
[20] M. H. Anderson, J. R. Ensher, M. R. Matthews, C. E. Wieman, and E. A. Cornell, Science **269**(5221), 198–201 (1995).
[21] K. B. Davis, M. O. Mewes, M. R. Andrews, N. J. van Druten, D. S. Durfee, D. M. Kurn, and W. Ketterle, Phys. Rev. Lett. **75**, 3969–3973 (1995).
[22] J. Mlynek, V. Balykin, and P. Meystre, Applied Physics B-Photophysics and Laser Chemistry **54**(5), 319–320 (1992).
[23] M. Aspelmeyer, S. Gröblacher, K. Hammerer, and N. Kiesel, J. Opt. Soc. Am. B **27**(6), A189–A197 (2010).
[24] P. Del'Haye, A. Schilesser, O. Arcizet, T. Wilken, R. Holzwarth, and T. J. Kippenberg, Nature **450**, 1214 (2007).
[25] T. J. Kippenberg and K. J. Vahala, Science **321**, 1172–1176 (2008).
[26] M. Li, W. H. P. Pernice, C. Xiong, T. Baehr-Jones, M. Hochberg, and H. X. Tang, Nature **456**(7221), 480–U28 (2008).
[27] M. Li, W. H. P. Pernice, and H. X. Tang, Nat. Photon. **3**(8), 464–468 (2009).
[28] P. B. Deotare, I. Bulu, I. W. Frank, Q. M. Quan, Y. N. Zhang, R. Ilic, and M. Loncar, Nat. Commun. **3** (2012).
[29] G. S. Wiederhecker, L. Chen, A. Gondarenko, and M. Lipson, Nature **462**(7273), 633–636 (2009).
[30] J. Rosenberg, Q. Lin, and O. Painter, Nat. Photon. **3**(8), 478–483 (2009).
[31] Q. Lin, J. Rosenberg, X. Jiang, K. J. Vahala, and O. Painter, Phys. Rev. Lett. **103**(10), 103601 (2009).
[32] M. Li, W. H. P. Pernice, and H. X. Tang, Phys. Rev. Lett. **103**(22) (2009).
[33] R. Thijssen, E. Verhagen, T. J. Kippenberg, and A. Polman, Nano Lett. **13**(7), 3293–3297 (2013).
[34] A. H. Safavi-Naeini, T. P. M. Alegre, M. Winger, and O. Painter, Appl. Phys. Lett. **97**(18) (2010).
[35] T. Corbitt, Y. Chen, E. Innerhofer, H. Müller-Ebhardt, D. Ottaway, H. Rehbein, D. Sigg, S. Whitcomb, C. Wipf, and N. Mavalvala, Phys. Rev. Lett. **98**, 150802 (2007).
[36] S. Zaitsev, A. K. Pandey, O. Shtempluck, and E. Buks, Phys. Rev. E **84**(4) (2011).
[37] M. Tomes and T. Carmon, Phys. Rev. Lett. **102**(11) (2009).
[38] G. Bahl, J. Zehnpfennig, M. Tomes, and T. Carmon, Nat. Comm. **2**, 403 (2011).
[39] E. Verhagen, S. Deleglise, S. Weis, A. Schliesser, and T. J. Kippenberg, Nature **482**(7383), 63–67 (2012).
[40] J. Chan, T. P. M. Alegre, A. H. Safavi-Naeini, J. T. Hill, A. Krause, S. Groblacher, M. Aspelmeyer, and O. Painter, Nature **478**(7367), 89–92 (2011).
[41] E. Gavartin, R. Braive, I. Sagnes, O. Arcizet, A. Beveratos, T. J. Kippenberg, and I. Robert-Philip, Phys. Rev. Lett. **106**(20) (2011).
[42] B. Ilic, S. Krylov, K. Aubin, R. Reichenbach, and H. G. Craighead, Appl. Phys. Lett. **86**(19) (2005).

[43] C. H. Metzger and K. Karrai, Nature **432**, 1002–1005 (2004).
[44] V. B. Braginsky and A. B. Manukin, Sov. Phys. JETP **25**, 653–655 (1967).
[45] L. Ding, C. Baker, P. Senellart, A. Lemaitre, S. Ducci, G. Leo, and I. Favero, Phys. Rev. Lett. **105**(26) (2010).
[46] M. L. Povinelli, M. Ibanescu, S. G. Johnson, and J. D. Joannopoulos, Appl. Phys. Lett. **85**, 1466–1468 (2004).
[47] C. H. Bui, J. Zheng, S. W. Hoch, L. Y. T. Lee, J. G. E. Harris, and C. Wei Wong, Appl. Phys. Lett. **100**(2), 021110 (2012).
[48] Z. Marcet, H. Hang, Z. B. Wang, S. J. Ng, T. Chan, and C. B. Chan, H., Phys. Rev. Lett. **112**, 045504 (2014).
[49] P. T. Rakich, P. Davids, and Z. Wang, Opt. Express **18**(14), 14439–14453 (2010).
[50] B. A. Kemp, J. A. Kong, and M. Grzegorczyk, Phys. Rev. E **75**, 053810 (2007).
[51] A. Mizrahi and Y. Fainman, Opt. Lett. **35**(20), 3405–3407 (2010).
[52] S. Weis, R. Riviere, S. Deleglise, E. Gavartin, O. Arcizet, A. Schliesser, and T. J. Kippenberg, Science **330**(6010), 1520–1523 (2010).
[53] J. J. Zheng, Y. Li, N. Goldberg, M. McDonald, X. S. Luan, A. Hati, M. Lu, S. Strauf, T. Zelevinsky, D. A. Howe, and C. W. Wong, Appl. Phys. Lett. **102**(14) (2013).
[54] A. G. Krause, M. Winger, T. D. Blasius, Q. Lin, and O. Painter, Nat. Photon. **6**(11), 768–772 (2012).
[55] G. Bahl, K. H. Kim, W. Lee, J. Liu, X. D. Fan, and T. Carmon, Nat. Commun. **4** (2013).
[56] K. J. Vahala, Nature **424**, 839–846 (2003).
[57] H. Rokhsari, T. J. Kippenberg, T. Carmon, and K. J. Vahala, Opt. Express **13**(14), 5293–5301 (2005).
[58] T. J. Kippenberg and K. J. Vahala, Opt. Express **15**(25), 17172–17205 (2007).
[59] M. Eichenfield, C. P. Michael, R. Perahia, and O. Painter, Nat. Photon. **1**(7), 416–422 (2007).
[60] A. M. Jayich, J. C. Sankey, B. M. Zwickl, C. Yang, J. D. Thompson, S. M. Girvin, A. A. Clerk, F. Marquardt, and J. G. E. Harris, New J. Phys. **10**(9), 095008 (2008).
[61] M. Eichenfield, J. Chan, R. M. Camacho, K. J. Vahala, and O. Painter, Nature **462**(7269), 78–82 (2009).
[62] D. V. Thourhout and J. Roels, Nat. Photon. **4**, 211–217 (2010).
[63] M. Li, W. H. P. Pernice, and H. X. Tang, Phys. Rev. Lett. **103**(22), 223901 (2009).
[64] K. Y. Fong, W. H. P. Pernice, M. Li, and H. X. Tang, Opt. Express **19**(16), 15098–15108 (2011).
[65] Y. Li, J. J. Zheng, J. Gao, J. Shu, M. S. Aras, and C. W. Wong, Opt. Express **18**(23), 23844–23856 (2010).
[66] J. J. Zheng, Y. Li, M. S. Aras, A. Stein, K. L. Shepard, and C. W. Wong, Appl. Phys. Lett. **100**(21) (2012).
[67] J. Ma and M. L. Povinelli, Appl. Phys. Lett. **97**, 151102 (2010).
[68] J. Chan, M. Eichenfield, R. Camacho, and O. Painter, Opt. Express **17**(5), 3802–3817 (2009).
[69] T. P. M. Alegre, R. Perahia, and O. Painter, Opt. Express **18**(8), 7872–7885 (2010).
[70] Q. Lin, J. Rosenberg, D. Chang, R. Camacho, M. Eichenfield, K. J. Vahala, and O. Painter, Nat. Photon. **4**(4), 236–242 (2010).
[71] A. H. Safavi-Naeini, T. P. Mayer Alegre, J. Chan, M. Eichenfield, M. Wigner, Q. Lin, J. T. Hill, D. E. Chang, and O. Painter, Nature **472**, 69–73 (2010).
[72] X. Yang, Y. Liu, R. F. Oulton, X. Yin, and X. Zhang, Nano Lett. **11**(2), 321–328 (2011).
[73] H. Li, J. W. Noh, Y. Chen, and M. Li, Opt. Express **21**(10), 11839–11851 (2013).
[74] K. Halterman, J. M. Elson, and S. Singh, Phys. Rev. B **72**(7), 075429 (2005).
[75] J. Kohoutek, D. Dey, A. Bonakdar, R. Gelfand, A. Sklar, O. G. Memis, and H. Mohseni, Nano Lett. **11**(8), 3378–3382 (2011).
[76] S. Groblacher, K. Hammerer, M. R. Vanner, and M. Aspelmeyer, Nature **460**(7256), 724–727 (2009).
[77] G. Anetsberger, O. Arcizet, Q. P. Unterreithmeier, R. Riviere, A. Schliesser, E. M. Weig, J. P. Kotthaus, and T. J. Kippenberg, Nat. Phys. **5**(12), 909–914 (2009).
[78] M. Li, W. H. P. Pernice, and H. X. Tang, Nat. Nanotech. **4**, 377–382 (2009).
[79] W. Suh, O. Solgaard, and S. Fan, J. Appl. Phys. **98**(3), 033102 (2005).
[80] T. Stomeo, M. Grande, G. Rainò, A. Passaseo, A. D'Orazio, R. Cingolani, A. Locatelli, D. Modotto, C. D. Angelis, and M. D. Vittorio, Opt. Lett. **35**(3), 411–413 (2010).
[81] H. Cai, K. J. Xu, A. Q. Liu, Q. Fang, M. B. Yu, G. Q. Lo, and D. L. Kwong, Appl. Phys. Lett. **100**(1) (2012).
[82] H. Cai, B. Dong, J. F. Tao, L. Ding, J. M. Tsai, G. Q. Lo, A. Q. Liu, and D. L. Kwong, Appl. Phys. Lett. **102**(2) (2013).
[83] M. C. Y. Hyang, Y. Zhou, and C. J. Chang-Hasnain, Nat. Phot. **2**, 180–184 (2008).
[84] D. Blocher, A. T. Zehnder, R. H. Rand, and S. Mukerji, Finite Elements in Analysis and Design **49**(1), 52–57 (2012).
[85] G. Jourdan, F. Comin, and J. Chevrier, Phys. Rev. Lett. **101**(13), 133904 (2008).
[86] W. H. P. Pernice, M. Li, and H. X. Tang, Appl. Phys. Lett. **105**, 014508 (2009).
[87] L. Troger and M. Reichling, Appl. Phys. Lett. **97**(21) (2010).
[88] S. Zaitsev, O. Shtempluck, E. Buks, and O. Gottlieb, Nonlinear Dynamics **67**, 859–883 (2012).
[89] D. Woolf, P. C. Hui, E. Iwase, M. Khan, A. W. Rodriguez, P. Deotare, I. Bulu, S. G. Johnson, F. Capasso, and M. Loncar, Opt. Express **21**(6), 7258–7275 (2013).
[90] A. H. Safavi-Naeini, J. Chan, J. T. Hill, T. P. M. Alegre, A. Krause, and O. Painter, Phys. Rev. Lett. **108**(3) (2012).
[91] M. L. Povinelli, M. Loncar, M. Ibanescu, E. J. Smythe, S. G. Johnson, F. Capasso, and J. D. Joannopoulos, Opt. Lett. **30**(22), 3042–3044 (2005).
[92] A. Oskooi, P. A. Favuzzi, Y. Kawakami, and S. Noda, Opt. Lett. **36**(23), 4638–4640 (2011).

[93] L. D. Landau and E. M. Lifshitz, Quantum Mechanics, 3rd edition (Butterworth-Heinemann, Oxford, 1977).
[94] A. W. Rodriguez, A. P. McCauley, P. C. Hui, D. Woolf, E. Iwase, F. Capasso, M. Loncar, and S. G. Johnson, Opt. Express **19**(3), 2225–2241 (2011).
[95] M. Povinelli, S. Johnson, M. Lonèar, M. Ibanescu, E. Smythe, F. Capasso, and J. Joannopoulos, Opt. Express **13**(20), 8286–8295 (2005).
[96] F. Riboli, A. Recati, M. Antezza, and I. Carusotto, Eur. Phys. J. D **46**, 157–164 (2008).
[97] P. T. Rakich, M. Popovic, and Z. Wang, Opt. Express **17**(20), 18116–18135 (2009).
[98] J. Roels, I. D. Vlaminck, L. Lagae, B. Maes, D. V. Throurout, and R. Baets, Nature Nano. **4**, 510–513 (2009).
[99] W. H. P. Pernice, M. Li, K. Y. Fong, and H. X. Tang, Opt. Express **17**(18), 16032–16037 (2009).
[100] D. Woolf, M. Loncar, and F. Capasso, Opt. Express **17**(22), 19996–20011 (2009).
[101] V. Yannopapas, Phys. Rev. B **78**(4), 045412 (2008).
[102] J. J. Xiao and C. T. Chan, J. Opt. Soc. Am. B **25**(9), 1553–1561 (2008).
[103] Y. G. Roh, T. Tanabe, A. Shinya, H. Taniyama, E. Kuramochi, S. Matsuo, T. Sato, and M. Notomi, Phys. Rev. B **81**(12), 121101 (2010).
[104] M. I. Antonoyiannakis and J. B. Pendry, Phys. Rev. B **60**(4), 2363–2374 (1999).
[105] M. T. H. Reid and S. G. Johnson, arXiv 1307.2966 (2014).
[106] X. Jiang, Q. Lin, J. Rosenberg, and K. V. and O. Painter, Opt. Express **17**(23), 20911–20919 (2009).
[107] M. Notomi, H. Taniyama, S. Mitsugi, and E. Kuramochi, Phys. Rev. Lett. **97**(2) (2006).
[108] H. Taniyama, M. Notomi, E. Kuramochi, T. Yamamoto, Y. Yoshikawa, Y. Torii, and T. Kuga, Phys. Rev. B **78**(16), 165129 (2008).
[109] Y. G. Roh, T. Tanabe, A. Shinya, H. Taniyama, E. Kuramochi, S. Matsuo, T. Sato, and M. Notomi, Phys. Rev. B **81**(12) (2010).
[110] E. Gavartin, P. Verlot, and T. J. Kippenberg, Nature Nanotechnology **7**(8), 509–514 (2012).
[111] F. Tian, G. Zhou, Y. Du, F. S. Chau, J. Deng, X. Tang, and R. Akkipeddi, Opt. Express **21**(15), 18398–18407 (2013).
[112] B. S. Song, S. Noda, T. Asano, and Y. Akahane, Nature Materials **4**(3), 207–210 (2005).
[113] A. R. M. Zain, N. P. Johnson, M. Sorel, and R. M. DeLaRue, Opt. Express **16**, 12084 (2008).
[114] M. Notomi, E. Kuramochi, and H. Taniyama, Opt. Express **16**, 11095 (2008).
[115] Y. Zhang, M. W. McCutcheon, I. B. Burgess, and M. Loncar, Opt. Lett. **34**, 17 (2009).
[116] Q. Quan and M. Loncar, Opt. Express **19**, 18529 (2011).
[117] J. Ng, C. T. Chan, P. Sheng, and Z. Lin, Opt. Lett. **30**(15), 1956–1958 (2005).
[118] P. T. Rakich, M. A. Popovic, M. Soljacic, and E. P. Ippen, Nat. Photon. **1**, 658–665 (2007).
[119] G. Wiederhecker, S. Manipatruni, S. Lee, and M. Lipson, Opt. Express **19**, 2782–2790 (2011).
[120] Y. Sun, T. P. White, and A. A. Sukhorukov, Opt. Lett. **37**(5), 785–787 (2012).
[121] P. A. Favuzzi, R. Bardoux, T. Asano, Y. Kawakami, and S. Noda, Opt. Express **20**(22), 24488–24495 (2012).
[122] P. A. Favuzzi, R. Bardoux, T. Asano, Y. Kawakami, and S. Noda, Opt. Express **21**(24), 29129–29139 (2013).
[123] J. Zhang, K. F. MacDonald, and N. I. Zheludev, Phys. Rev. B **85**(20) (2012).
[124] J. Zhang, K. F. MacDonald, and N. I. Zheludev, Light: Science & Applications **2**, 96 (2013).
[125] V. Ginis, P. Tassin, C. M. Soukoulis, and I. Veretennicoff, Phys. Rev. Lett. **110**(5) (2013).
[126] A. Mizrahi and L. Schächter, Opt. Lett. **32**(6), 692–694 (2007).
[127] D. Woolf, M. A. Kats, and F. Capasso, Opt. Lett. **39**(3), 517–520 (2014).
[128] J. D. Joannopoulos, S. G. Johnson, J. N. Winn, and R. D. Meade, Photonic Crystals: Molding the Flow of Light, second edition (Princeton University Press, February 2008).
[129] V. Liu, M. Povinelli, and S. Fan, Opt. Express **17**(24), 21897–21909 (2009).
[130] R. Zhao, P. Tassin, T. Koschny, and C. M. S. Koulis, Opt. Express **18**(25), 25665–25676 (2010).
[131] M. Lapine, I. V. Shadrivov, D. A. Powerll, and Y. Kivshar, Nat. Mat. **11**, 30–33 (2011).
[132] W. Zhang and G. Wang, Plasmonics (2014).
[133] T. W. Lu and P. T. Lee, Opt. Express **17**(3), 1518–1526 (2009).
[134] P. C. Hui, D. Woolf, E. Iwase, Y. I. Sohn, D. Ramos, M. Khan, A. W. Rodriguez, S. G. Johnson, F. Capasso, and M. Loncar, Appl. Phys. Lett. **103**(2) (2013).
[135] L. Gao, K. Shigeta, A. Vazquez-Guardado, C. J. Progler, G. R. Bogart, J. A. Rogers, and D. Chanda, ACS Nano (2014).
[136] C. M. Soukoulis and M. Wegener, Nat. Photon. **5**(9), 523–530 (2011).
[137] Y. Zhao, M. Belkin, and A. Alù, Nat. Commun. **3**, 870 (2012).
[138] R. Maas, J. Parsons, N. Engheta, and A. Polman, Nat. Photon. (2013).
[139] K. Kusaka, H. Kurosawa, S. Ohno, Y. Sakaki, K. Nakayama, Y. Moritake, and T. Ishihara, arXiv preprint arXiv:1405.5395 (2014).
[140] M. Bagheri, M. Poot, M. Li, W. P. H. Pernice, and H. X. Tang, Nature Nanotechnology **6**(11), 726–732 (2011).
[141] I. W. Frank, P. B. Deotare, M. W. McCutcheon, and M. Lončar, Opt. Express **18**(8), 8705–8712 (2010).
[142] M. Winger, T. D. Blasius, T. P. M. Alegre, A. H. Safavi-Naeini, S. Meenehan, J. Cohen, S. Stobbe, and O. Painter, Opt. Express **19**(25), 24905–24921 (2011).
[143] M. Poot and H. X. Tang, Appl. Phys. Lett. **104**(6) (2014).
[144] X. Sun, X. Zhang, M. Poot, C. Xiong, and H. X. Tang, Appl. Phys. Lett. **101**(22), 221116 (2012).
[145] E. Iwase, P. C. Hui, D. Woolf, A. W. Rodriguez, S. G. Johnson, F. Capasso, and M. Lončar, Journal of

Micromechanics and Microengineering **22**(6), 065028 (2012).
[146] L. Midolo, S. Yoon, F. Pagliano, T. Xia, F. van Otten, M. Lermer, S. Höfling, and A. Fiore, Opt. Express **20**(17), 19255–19263 (2012).
[147] P. Rath, S. Khasminskaya, C. Nebel, C. Wild, and W. H. Pernice, Nat. Commun. **4**, 1690 (2013).
[148] K. Y. Fong, W. Pernice, M. Li, and H. Tang, Appl. Phys. Lett. **97**(7), 073112 (2010).
[149] S. Hadzialic, S. Kim, A. F. Sarioglu, A. S. Sudbø, and O. Solgaard, Photonics Technology Letters, IEEE **22**(16), 1196–1198 (2010).
[150] B. Dong, J. Huang, H. Cai, P. Kropelnicki, A. Randles, Y. Gu, and A. Liu, An all optical shock sensor based on buckled doubly-clamped silicon beam, Jan 2014.
[151] V. Intaraprasonk and S. H. Fan, Appl. Phys. Lett. **98**(24) (2011).
[152] F. F. Liu, S. Alaie, Z. C. Leseman, and M. Hossein-Zadeh, Opt. Express **21**(17), 19555–19567 (2013).
[153] Y. X. Liu, H. X. Miao, V. Aksyuk, and K. Srinivasan, Opt. Express **20**(16), 18268–18280 (2012).
[154] H. X. Miao, K. Srinivasan, and V. Aksyuk, New J. Phys. **14** (2012).
[155] K. H. Kim, G. Bahl, W. Lee, J. Liu, M. Tomes, X. D. Fan, and T. Carmon, Light-Science and Applications **2** (2013).
[156] M. Oudich, S. El-Jallal, Y. Pennec, B. Djafari-Rouhani, J. Gomis-Bresco, D. Navarro-Urrios, C. M. S. Torres, A. Martínez, and A. Makhoute, Phys. Rev. B **89**(24), 245122 (2014).
[157] S. El-Jallal, M. Oudich, Y. Pennec, B. Djafari-Rouhani, V. Laude, J. C. Beugnot, A. Martínez, J. M. Escalante, and A. Makhoute, Phys. Rev. B **88**(20), 205410 (2013).
[158] F. L. Hsiao, C. Y. Hsieh, H. Y. Hsieh, and C. C. Chiu, Appl. Phys. Lett. **100**(17), 171103 (2012).
[159] A. H. Safavi-Naeini and O. Painter, New J. Phys. **13** (2011).
[160] L. Tian and H. L. Wang, Phys. Rev. A **82**(5) (2010).
[161] J. T. Hill, A. H. Safavi-Naeini, J. Chan, and O. Painter, Nat. Commun. **3** (2012).
[162] M. Davanco, J. Chan, A. H. Safavi-Naeini, O. Painter, and K. Srinivasan, Opt. Express **20**(22), 24394–24410 (2012).
[163] M. Davanco, S. Ates, Y. Liu, and K. Srinivasan, Appl. Phys. Lett. **104**(4) (2014).
[164] Y. X. Liu, M. Davanco, V. Aksyuk, and K. Srinivasan, Phys. Rev. Lett. **110**(22) (2013).
[165] J. Bochmann, A. Vainsencher, D. D. Awschalom, and A. N. Cleland, Nature Physics **9**(11), 712–716 (2013).
[166] H. Rokhsari, M. Hossein-Zadeh, A. Hajimiri, and K. Vahala, Appl. Phys. Lett. **89**(26) (2006).
[167] M. Hossein-Zadeh, H. Rokhsari, A. Hajimiri, and K. J. Vahala, Phys. Rev. A **74**(2) (2006).
[168] M. Hossein-Zadeh and K. J. Vahala, Appl. Phys. Lett. **93**(19) (2008).
[169] M. Hossein-Zadeh and K. J. Vahala, IEEE Photo. Tech. Lett. **20**(1-4), 234–236 (2008).
[170] M. Hossein-Zadeh and K. J. Vahala, IEEE J. Quantum Electron. **16**(1), 276–287 (2010).
[171] F. Liu and M. Hossein-Zadeh, Opt. Commun. **294**, 338–343 (2013).
[172] F. F. Liu and M. Hossein-Zadeh, J. Lightwave Tech. **32**(2), 309–317 (2014).
[173] F. M. Serry, D. Walliser, and M. G. Jordan, J. Appl. Phys. **84**, 2501–2506 (1998).
[174] E. Buks and M. L. Roukes, Europhys. Lett. **54**(2), 220 (2001).
[175] F. Capasso, J. N. Munday, D. Iannuzzi, and H. B. Chan, IEEE J. Select. Top. Quant. Electron. **13**(2), 400–415 (2007).
[176] C. Genet, A. Lambrecht, and S. Reynaud, Eur. Phys. J. Special Topics **160**, 183–193 (2008).
[177] H. B. G. Casimir, Proc. K. Ned. Akad. Wet. **51**, 793–795 (1948).
[178] E. M. Lifshitz, Sov. Phys. JETP **2**, 73–84 (1956).
[179] I. E. Dzyaloshinskiĭ, E. M. Lifshitz, and L. P. Pitaevskiĭ, Adv. Phys. **10**(38), 165–209 (1961).
[180] G. Plunien, B. Muller, and W. Greiner, Phys. Rep. **134**(87), 87–193 (1986).
[181] L. Spruch, Science **272**, 1452–1455 (1996).
[182] M. Kardar and R. Golestanian, Rev. Mod. Phys. **71**(4), 1233–1245 (1999).
[183] K. A. Milton, The Casimir Effect: Physical Manifestations of Zero-Point Energy (Singapore: World Scientific, 2001).
[184] K. A. Milton, J. Phys. A **37**, R209–R277 (2004).
[185] M. Bordag, U. Mohideen, and V. M. Mostepanenko, Phys. Rep. **353**, 1–205 (2001).
[186] A. Lambrecht, Physics World **15**, 29–32 (2002).
[187] S. K. Lamoreaux, Rep. Prog. Phys. **68**, 201–236 (2005).
[188] R. Onofrio, New J. Phys. **8**, 237 (2006).
[189] S. K. Lamoreaux, Phys. Today **60**, 40–45 (2007).
[190] P. Ball, Nature **447**, 772–774 (2007).
[191] S. Y. Buhmann and D. G. Welsch, Prog. Quant. Elec. **31**(2), 51–130 (2007).
[192] D. A. R. Dalvit, P. Milonni, D. Roberts, and F. da Rosa (eds.), Lecture Notes in Physics (Springer-Verlag, 2011).
[193] S. Y. Buhmann, Dispersion Forces I: Macroscopic Quantum Electrodynamics and Ground-State Casimir, Casimir–Polder and van der Waals Forces, Springer Tract in Modern Physics, Vol. 247 (Springer, 2012).
[194] M. T. H. Reid, A. W. Rodriguez, and S. G. Johnson, Proc. IEEE **101**(2), 531–545 (2013).
[195] K. A. Milton, E. K. Abalo, P. Parashar, N. Pourtolami, I. Brevik, and S. A. Ellingsen, J. Phys. A: Math. Theor. **45**, 374006 (2012).
[196] V. N. Marachevsky, J. Phys. A: Math. Theor. **45**, 374021 (2012).
[197] F. London, Trans. Faraday Soc. **33**, 8–26 (1937).
[198] J. Mahanty and B. W. Ninham, Dispersion Forces (Academic Press, London, 1976).
[199] A. V. Parsegian, Van der Waals Forces: A Handbook for Biologists, Chemists, Engineers, and Physicists (Cambridge University Press, NY, 2006).

[200] H. B. G. Casimir and D. Polder, Phys. Rev. **13**(4), 360–372 (1948).
[201] F. Intravaia and A. Lambrecht, Phys. Rev. Lett. **94**, 110404 (2005).
[202] N. G. van Kampen, B. R. Nijober, and K. Schram, Phys. Lett. A **26A**(7), 307–308 (1968).
[203] C. Genet, A. Lambrecht, and S. Reynaud, Phys. Rev. A **67**(4), 043811 (2003).
[204] S. J. Van Enk, J. Mod. Opt. **42**(2), 321–338 (1995).
[205] F. Intravaia, C. Henkel, and A. Lambrecht, Phys. Rev. A **76**, 033820 (2007).
[206] E. M. Lifshitz and L. P. Pitaevskii, Statistical Physics: Part 2 (Pergamon, Oxford, 1980).
[207] E. Gerlach, Phys. Rev. B **4**, 393–396 (1971).
[208] N. Graham, M. Quandt, and H. Weigel, Spectral Methods in Quantum Field Theory (Springer-Verlag, Berlin, 2009).
[209] W. L. Mochan and C. Villarreal, New J. Phys. **8**, 242 (2006).
[210] P. S. Davids, F. Intravaia, F. S. S. Rosa, and D. A. R. Dalvit, Phys. Rev. A **82**(6), 062111 (2010).
[211] W. Eckhardt, Phys. Rev. A **29**(4), 1991–2003 (1984).
[212] L. P. Pitaevskiĭ, Phys. Rev. A **73**, 047801 (2006).
[213] T. G. Philbin, New J. Phys. **13**, 063026 (2011).
[214] M. T. H. Reid, J. White, and S. G. Johnson, Phys. Rev. A **88**, 022514 (2013).
[215] M. T. Jaekel and S. Reynaud, J. Physique I **1**, 1395–1409 (1991).
[216] F. Zhou and L. Spruch, Phys. Rev. A **52**(1), 297–310 (1995).
[217] G. L. Klimchitskaya, U. Mohideen, and V. M. Mostepanenko, Phys. Rev. A **61**, 062107 (2000).
[218] M. S. Tomaš, Phys. Rev. A **66**, 052103 (2002).
[219] B. V. Derjaguin, Kolloid Z. **69**, 155 (1934).
[220] K. A. Milton, P. Parashar, and J. Wagner, Phys. Rev. Lett. **101**, 160402 (2008).
[221] K. A. Milton and J. Wagner, Journal of Physics A: Mathematical and Theoretical **41**(15), 155402 (2008).
[222] R. Golestanian, Phys. Rev. A **80**(1), 012519 (2009).
[223] F. S. S. Rosa, J. Phys. Conf. Ser. **161**, 012039 (2009).
[224] A. P. McCauley, R. Zhao, M. T. H. Reid, A. W. Rodriguez, J. Zhuo, F. S. S. Rosa, J. D. Joannopoulos, D. A. R. Dalvit, C. M. Soukoulis, and S. G. Johnson, Phys. Rev. B **82**, 165108 (2010).
[225] B. V. Derjaguin, I. I. Abrikosova, and E. M. Lifshitz, Q. Rev. Chem. Soc. **10**, 295–329 (1956).
[226] M. Bordag, Phys. Rev. D **73**, 125018 (2006).
[227] T. Emig, R. L. Jaffe, M. Kardar, and A. Scardicchio, Phys. Rev. Lett. **96**, 080403 (2006).
[228] A. F. Bitbol, A. Canaguier-Durand, A. Lambrecht, and S. Reynaud, Phys. Rev. B **87**, 045413 (2013).
[229] M. Tajmar, Intl. J. Mod. Phys. C **15**(10), 1387–1395 (2004).
[230] R. Sedmik, I. Vasiljevich, and M. Tajmar, J. Computer-Aided Mat. Des. **14**(1), 119–132 (2007).
[231] M. Schaden and L. Spruch, Phys. Rev. A **58**, 935–953 (1998).
[232] R. Balian and B. Duplantier, Ann. Phys. **112**, 165–208 (1978).
[233] T. Emig, A. Hanke, R. Golestanian, and M. Kardar, Phys. Rev. Lett. **87**, 260402 (2001).
[234] A. Lambrecht, P. A. Maia Neto, and S. Reynaud, New J. Phys. **8**(243), 1–25 (2006).
[235] M. F. Maghrebi, Phys. Rev. D **83**, 045004 (2011).
[236] R. L. Jaffe and A. Scardicchio, Phys. Rev. Lett. **92**, 070402 (2004).
[237] A. Scardicchio and R. L. Jaffe, Nuclear Physics B. **704**(3), 552–582 (2005).
[238] C. D. Fosco, F. C. Lombardo, and F. D. Mazzitelly, Phys. Rev. D. **84**, 105031 (2011).
[239] L. P. Teo, M. Bordag, and V. Nikolaev, Phys. Rev. D. **84**, 125037 (2011).
[240] G. Bimonte, T. Emig, R. L. Jaffe, and M. Kardar, EPL **97**, 50001 (2012).
[241] G. Bimonte, T. Emig, and M. Kardar, Appl. Phys. Lett. **100**, 074110 (2012).
[242] L. P. Teo, Phys. Rev. D. **88**, 045019 (2013).
[243] F. D. Mazitelli, D. A. R. Dalvit, and F. C. Lobardo, New J. Phys. **8**(240), 1–21 (2006).
[244] D. A. R. Dalvit, F. C. Lombardo, F. D. Mazzitelli, and R. Onofrio, Phys. Rev. A **74**, 020101(R) (2006).
[245] T. Emig, N. Graham, R. L. Jaffe, and M. Kardar, Phys. Rev. Lett. **99**, 170403 (2007).
[246] O. Kenneth and I. Klich, Phys. Rev. B **78**, 014103 (2008).
[247] A. Lambrecht and V. I. Marachevsky, Phys. Rev. Lett. **101**, 160403 (2008).
[248] S. J. Rahi, T. Emig, N. Graham, R. L. Jaffe, and M. Kardar, Phys. Rev. D **80**, 085021 (2009).
[249] A. Rodriguez, M. Ibanescu, D. Iannuzzi, J. D. Joannopoulos, and S. G. Johnson, Phys. Rev. A **76**(3), 032106 (2007).
[250] H. Gies, K. Langfeld, and L. Moyaerts, J. High Energy Phys. **6**, 018 (2003).
[251] T. Emig, Europhys. Lett. **62**, 466 (2003).
[252] R. Büscher and T. Emig, Phys. Rev. A **69**, 062101 (2004).
[253] H. Gies and K. Klingmuller, Phys. Rev. D **74**, 045002 (2006).
[254] H. Reid, J. White, and S. G. Johnson, Phys. Rev. A. Rapid. Comm. **84**, 010503 (2011).
[255] K. A. Milton, P. Parashar, J. Wagner, and C. Pelaez, J. Vac. Sci. Tech. B **28**(3), C4A8–C4A16 (2010).
[256] S. Pasquali and A. C. Maggs, J. Chem. Phys. **129**, 014703 (2008).
[257] S. Pasquali and A. C. Maggs, Phys. Rev. A. **79**, 020102(R) (2009).
[258] A. W. Rodriguez, A. P. McCauley, J. D. Joannopoulos, and S. G. Johnson, Phys. Rev. A **80**(1), 012115 (2009).
[259] A. P. McCauley, A. W. Rodriguez, J. D. Joannopoulos, and S. G. Johnson, Phys. Rev. A **81**, 012119 (2010).
[260] M. T. H. Reid, A. W. Rodriguez, J. White, and S. G. Johnson, Phys. Rev. Lett. **103**(4), 040401 (2009).
[261] J. Xiong and W. C. Chew, Appl. Phys. Lett. **95**, 154102 (2009).

[262] J. L. Xiong, M. S. Tong, P. Atkins, and W. C. Chew, Phys. Lett. A **374**(25), 2517–2520 (2010).
[263] P. R. Atkins, Q. I. Dai, W. E. I. Sha, and W. C. Chew, Prog. Electromag. Research **142**, 615–624 (2013).
[264] S. K. Lamoreaux, Phys. Rev. Lett. **78**, 5 (1997).
[265] W. Kim, A. Sushkov, D. Dalvit, and S. Lamoreaux, Phys. Rev. Lett. **103**(6), 060401 (2009).
[266] A. O. Sushkov, W. J. Kim, D. A. R. Dalvit, and S. K. Lamoreaux, Nat. Phys. **7**, 230–233 (2011).
[267] U. Mohideen and A. Roy, Phys. Rev. Lett. **81**, 4549–4552 (1998).
[268] B. W. Harris, F. Chen, and M. U., Phys. Rev. A **62**, 052109 (2000).
[269] C. C. Chang, A. Banishev, G. Klimchitskaya, V. Mostepanenko, and U. Mohideen, Phys. Rev. Lett. **107**(9), 090403 (2011).
[270] A. A. Banishev, J. Wagner, T. Emig, R. Zandi, and U. Mohideen, Phys. Rev. B **89**, 235436 (2014).
[271] G. Torricelli, S. Thornton, C. Binns, I. Pirozhenko, and A. Lambrecht, Journal of Vacuum Science & Technology B **28**(3), C4A30–C4A35 (2010).
[272] G. Torricelli, I. Pirozhenko, S. Thornton, A. Lambrecht, and C. Binns, EPL (Europhysics Letters) **93**(5), 51001 (2011).
[273] J. Laurent, H. Sellier, A. Mosset, S. Huant, and J. Chevrier, Phys. Rev. B **85**(3), 035426 (2012).
[274] C. C. Chang, A. Banishev, R. Castillo-Garza, G. Klimchitskaya, V. Mostepanenko, and U. Mohideen, Phys. Rev. B **85**(16), 165443 (2012).
[275] A. Banishev, C. C. Chang, G. Klimchitskaya, V. Mostepanenko, and U. Mohideen, Phys. Rev. B **85**(19), 195422 (2012).
[276] A. A. Banishev, G. L. Klimchitskaya, V. M. Mostepanenko, and U. Mohideen, Phys. Rev. Lett. **110**, 137401 (2013).
[277] A. A. Banishev, H. Wen, J. Xu, R. K. Kawakami, G. L. Klimchitskaya, V. M. Mostepanenko, and U. Mohideen, Phys. Rev. B **87**, 205433 (2013).
[278] H. B. Chan, V. A. Aksyuk, R. N. Kleinman, D. J. Bishop, and F. Capasso, Science **291**, 1941–1944 (2001).
[279] M. Sparnaay, Physica **24**(6-10), 751–764 (1958).
[280] S. K. Lamoreaux, Phys. Rev. Lett. **78**, 5–8 (1997).
[281] G. Bressi, G. Carugno, R. Onofrio, and G. Ruoso, Phys. Rev. Lett. **88**, 041804 (2002).
[282] S. de Man, K. Heeck, R. J. Wijngaarden, and D. Iannuzzi, Phys. Rev. Lett. **103**, 040402 (2009).
[283] S. de Man, K. Heeck, and D. Iannuzzi, Phys. Rev. A **82**, 062512 (2010).
[284] G. Jourdan, A. Lambrecht, F. Comin, and J. Chevrier, Europhys. Lett. **85**(3), 31001 (2009).
[285] H. B. Chan, V. A. Aksyuk, R. N. Kleinman, D. J. Bishop, and F. Capasso, Phys. Rev. Lett. **87**, 211801 (2001).
[286] R. S. Decca, D. Lopez, E. Fischbach, and D. E. Krause, Phys. Rev. Lett. **91**, 050402 (2003).
[287] R. Decca, E. Fischbach, G. Klimchitskaya, D. Krause, D. López, and V. Mostepanenko, Physical Review D **68**(11), 116003 (2003).
[288] H. B. Chan, Y. Bao, J. Zou, R. A. Cirelli, F. Klemens, W. M. Mansfield, and C. S. Pai, Phys. Rev. Lett. **101**, 030401 (2008).
[289] F. Intravaia, S. Koev, I. W. Jung, A. A. Talin, P. S. Davids, R. S. Decca, A. Aksyuk, D. A. R. Dalvit, and D. Lopez, Nat. Comm. **4**, 2515 (2013).
[290] J. Zho, Z. Marcet, A. W. Rodriguez, M. T. H. Reid, A. P. McCauley, I. I. Kravchenko, T. Lu, Y. Bao, S. G. Johnson, and H. B. Chan, Nat. Comm. **4**, 1845 (2013).
[291] S. Lamoreaux (2010), Preprint at http://arxiv.org/abs/1008.3640 (2010).
[292] Q. Wei, D. A. R. Dalvit, F. C. Lombardo, F. D. Mazzitelli, and O. Onofrio, Phys. Rev. A **81**, 052115 (2010).
[293] S. de Man, K. Heeck, R. J. Wijngaarden, and D. Iannuzzi, J. Vac. Sci. Technol. B **28** (2010).
[294] D. Garcia-Sanchez, K. Y. Fong, H. Bhaskaran, S. Lamoreaux, and H. X. Tang, Phys. Rev. Lett. **109**, 027202 (2012).
[295] C. Speake and C. Trenkel, Phys. Rev. Lett. **90**(16), 160403 (2003).
[296] M. Bordag, G. L. Klimchitskaya, U. Mohideen, and V. M. Mostapanenko, Advances in the Casimir Effect (Oxford University Press, Oxford, UK, 2009).
[297] W. J. Kim, A. O. Sushkov, D. A. R. Dalvit, and S. K. Lamoreaux, Phys. Rev. A **81**(2), 022505 (2010).
[298] R. Behunin, F. Intravaia, D. Dalvit, P. M. Neto, and S. Reynaud, Phys. Rev. A **85**(1), 012504 (2012).
[299] R. Behunin, Y. Zeng, D. Dalvit, and S. Reynaud, Phys. Rev. A **86**(5), 052509 (2012).
[300] D. Garcia-Sanchez, K. Y. Fong, H. Bhaskaran, S. Lamoreaux, and H. X. Tang, Review of Scientific Instruments **84**(1), 015115 (2013).
[301] T. Ederth, Phys. Rev. A **62**, 062104 (2000).
[302] C. Genet, A. Lambrecht, P. Maia Neto, and S. Reynaud, Europhys. Lett. **62**, 484 (2003).
[303] P. J. van Zwol, G. Palasantzas, and J. T. M. De Hosson, Phys. Rev. B **77**, 075412 (2008).
[304] W. Broer, G. Palasantzas, J. Knoester, and V. B. Svetovoy, Phys. Rev. B **85**, 155410 (2012).
[305] H. B. Chan, Y. Bao, J. Zou, R. Cirelli, F. Klemens, W. Mansfield, and C. Pai, International Journal of Modern Physics A **25**(11), 2212–2222 (2010).
[306] G. Torricelli, P. J. van Zwol, O. Shpak, G. Palasantzas, V. B. Svetovoy, C. Binns, B. J. Kooi, P. Jost, and M. Wuttig, Advanced Functional Materials **22**(17), 3729–3736 (2012).
[307] I. Pirozhenko, A. Lambrecht, and V. B. Svetovoy, New J. Phys. **8**(10), 238 (2006).
[308] V. Svetovoy, P. Van Zwol, G. Palasantzas, and J. T. M. De Hosson, Phys. Rev. B **77**(3), 035439 (2008).
[309] P. J. van Zwol, G. Palasantzas, and J. T. M. De Hosson, Phys. Rev. B **79**, 195428 (2009).
[310] P. J. van Zwol and G. Palasantzas, Phys. Rev. A **81**, 062502 (2010).
[311] R. L. Olmon, B. Slovick, T. W. Johnson, D. Shelton, S. H. Oh, G. D. Boreman, and M. B. Raschke, Phys. Rev. B **86**(23), 235147 (2012).

[312] M. Sedighi, V. B. Svetovoy, W. H. Broer, and G. Palasantzas, Phys. Rev. B **89**, 195440 (2014).
[313] G. Torricelli, P. van Zwol, O. Shpak, C. Binns, G. Palasantzas, B. Kooi, V. Svetovoy, and M. Wuttig, Phys. Rev. A **82**(1), 010101 (2010).
[314] A. W. Rodriguez, D. Woolf, P. C. Hui, E. Iwãse, A. P. McCauley, F. Capasso, and S. G. LoncarMarko and Johnson, Appl. Phys. Lett. **98**(19), 194105 (2011).
[315] W. H. P. Pernice, M. Li, D. Garcia-Sanchez, and H. X. Tang, Opt. Express **18**(12), 12615–12621 (2010).
[316] M. S. Nawazuddin, T. Lammerink, R. Wiegerink, and M. Elwenspoek, Journal of Micromechanics and Microengineering **20**(6), 064005 (2010).
[317] C. Yamarthy and S. McNamara, Design of a mems sensor to detect the casimir force, in: Nano/Micro Engineered and Molecular Systems, 2009. NEMS 2009. 4th IEEE International Conference on, (2009), pp. 645–648.
[318] T. Emig, A. Hanke, R. Golestanian, and M. Kardar, Phys. Rev. A **67**, 022114 (2003).
[319] A. Rodriguez, M. Ibanescu, D. Iannuzzi, F. Capasso, J. D. Joannopoulos, and S. G. Johnson, Phys. Rev. Lett. **99**(8), 080401 (2007).
[320] A. W. Rodriguez, J. D. Joannopoulos, and S. G. Johnson, Phys. Rev. A **77**(6), 062107 (2008).
[321] M. Levin, A. P. McCauley, A. W. Rodriguez, M. T. H. Reid, and S. G. Johnson, Phys. Rev. Lett. **105**, 090403 (2010).
[322] T. H. Boyer, Phys. Rev. **174**, 1764–1776 (1968).
[323] K. A. Milton, L. L. DeRaad Jr., and J. Schwinger, Ann. Phys. **115**, 388–403 (1978).
[324] I. Brevick and G. Einevoll, Phys. Rev. D **37**, 2977 (1987).
[325] R. M. Cavalcanti, Phys. Rev. D **69**, 065015 (2004).
[326] M. P. Hertzberg, R. L. Jaffe, M. Kardar, and A. Scardicchio, Phys. Rev. D **76**(4), 045016 (2007).
[327] V. M. Marachevsky, J. Phys. A: Math. Theor. **41**, 164007 (2008).
[328] O. Kenneth, I. Klich, A. Mann, and M. Revzen, Phys. Rev. Lett. **89**(3), 033001 (2002).
[329] R. L. Jaffe, AIP Conf. Proc. **687**(1), 3–12 (2003).
[330] N. Graham, M. Quandt, and H. Weigel, Phys. Lett. B. **726**, 846–849 (2013).
[331] H. Gies and K. Klingmuller, Phys. Rev. Lett. **96**, 220401 (2006).
[332] P. A. Maia Neto, A. Lambrecht, and S. Reynaud, Phys. Rev. A **78**, 012115 (2008).
[333] T. Emig, J. Stat. Mech. Theory Exp. **2008**(04), P04007 (2008).
[334] S. J. Rahi, T. Emig, R. L. Jaffe, and M. Kardar, Phys. Rev. A **78**, 012104 (2008).
[335] T. Emig, N. Graham, L. R. Jaffe, and M. Kardar, Phys. Rev. A **79**, 054901 (2009).
[336] N. Graham, A. Shpunt, T. Emig, S. J. Rahi, R. L. Jaffe, and M. Kardar, Phys. Rev. D. **81**, 061701(R) (2010).
[337] N. Graham, Phys. Rev. D. **87**, 105004 (2013).
[338] A. Weber and H. Gies, Phys. Rev. Lett. **105**(4), 040403 (2010).
[339] A. Weber and H. Gies, Phys. Rev. D **82**, 125019 (2010).
[340] M. F. Maghrebi, S. J. Rahi, T. Emig, N. Graham, R. L. Jaffe, and M. Kardar, Proc. Nat. Acad. Sci. **108**, 6867–6871 (2011).
[341] H. C. Chiu, G. L. Klimchitskaya, V. N. Marachevsky, V. M. Mostepanenko, and U. Mohideen, Phys. Rev. B **81**(11), 115417 (2010).
[342] A. Roy, and U. Mohideen, Phys. Rev. Lett. **82**, 4380 (1999).
[343] R. Büscher and T. Emig, Phys. Rev. A **69**(6), 062101 (2004).
[344] R. Guerout, J. Lussange, H. B. Chan, A. Lambrecht, and S. Reynaud, Phys. Rev. A **87**, 052514 (2013).
[345] J. Lussange, R. Guerout, and A. Lambrecht, Phys. Rev. A. **86**, 062502 (2012).
[346] J. Munday, F. Capasso, and V. A. Parsegian, Nature **457**, 170–173 (2009).
[347] T. Emig, A. Hanke, R. Golestanian, and M. Kardar, Phys. Rev. Lett. **87**, 260402 (2001).
[348] R. B. Rodrigues, P. A. M. Neto, A. Lambrecht, and S. Reynaud, Phys. Rev. Lett. **96**, 100402 (2006).
[349] T. Emig, Phys. Rev. Lett. **98**, 160801 (2007).
[350] M. Miri and R. Golestanian, APL **92**, 113103 (2008).
[351] G. Bimonte, Phys. Rev. Lett. **112**, 240401 (2014).
[352] I. Brevik and J. S. Hoye, Eur. J. Phys. **35**, 015012 (2014).
[353] F. W. DelRio, M. P. de Boer, J. A. Knaap, E. D. J. Reedy, P. J. Clews, and M. L. Dunn, Nature Materials **4**, 629–634 (2005).
[354] G. L. Klimchitskaya and Y. V. Pavlov, Int. J. Mod. Phys. A **11**(20), 3723 (1996).
[355] P. A. Maia Neto, A. Lambrecht, and S. Reynaud, Europhys. Lett. **69**, 924 (2005).
[356] G. Palasantzas, J. Appl. Phys. **97**, 126104 (2005).
[357] R. Decca, D. LÃ³pez, E. Fischbach, G. Klimchitskaya, D. Krause, and V. Mostepanenko, Annals of Physics **318**(1), 37–80 (2005).
[358] W. Broer, G. Palasantzas, J. Knoester, and V. B. Svetovoy, Phys. Rev. B **87**, 125413 (2013).
[359] M. Kruger, V. A. Golyk, G. Bimonte, and M. Kardar, EPL **104**, 41001 (2013).
[360] S. Zaheer, A. W. Rodriguez, S. G. Johnson, and R. L. Jaffe, Phys. Rev. A **76**(6), 063816 (2007).
[361] P. Rodriguez-Lopez, S. J. Rahi, and T. Emig, Phys. Rev. A **80**(2), 022519 (2009).
[362] A. W. Rodriguez, A. P. McCauley, D. Woolf, F. Capasso, J. D. Joannopoulos, and S. G. Johnson, Phys. Rev. Lett. **104**(16), 160402 (2010).
[363] A. W. Rodriguez, D. Woolf, A. P. McCauley, F. Capasso, and S. G. Johnson, Phys. Rev. Lett. **105**, 060401 (2010).
[364] A. W. Rodriguez, M. T. H. Reid, F. Intravaia, A. Woolf, D. A. R. Dalvit, F. Capasso, and S. G. Johnson, Phys. Rev. Lett. **111**, 180402 (2013).
[365] T. H. Boyer, Phys. Rev. A **9**, 2078–2084 (1974).
[366] U. Leonhardt and T. G. Philbin, New J. Phys. **9**, 254 (2007).
[367] F. S. S. Rosa, D. A. R. Dalvit, and P. W. Milonni, Phys. Rev. Lett. **100**, 183602 (2008).

[368] R. Zhao, J. Zhou, T. Koschny, E. N. Economou, and C. M. Soukoulis, Phys. Rev. Lett. **103**, 103602 (2009).
[369] P. Rodriguez-Lopez and A. G. Grushin, Phys. Rev. Lett. **112**, 056804 (2014).
[370] H. A. Stone and S. Kim, AIChE J. **47**(6), 1250–1254 (2001).
[371] A. W. Rodriguez, J. Munday, D. Davlit, F. Capasso, J. D. Joannopoulos, and S. G. Johnson, Phys. Rev. Lett. **101**(19), 190404 (2008).
[372] A. W. Rodriguez, A. P. McCauley, D. Woolf, F. Capasso, J. D. Joannopoulos, and S. G. Johnson, Phys. Rev. Lett. **104**(16), 160402 (2010).
[373] A. P. McCauley, F. S. S. Rosa, A. W. Rodriguez, J. D. Joannopoulos, D. A. R. Dalvit, and S. G. Johnson, Phys. Rev. A **83**, 052503 (2011).
[374] A. D. Phan and N. A. Viet, Phys. Rev. A **84**, 062503 (2011).
[375] M. Dou, F. Lou, M. Boström, I. Brevik, and C. Persson, Phys. Rev. B **89**, 201407 (2014).
[376] A. G. Grushin and A. Cortijo, PRL **106**, 020403 (2011).
[377] C. Raabe and D. G. Welsch, The European Physical Journal Special Topics **160**(1), 371–381 (2007).
[378] C. Henkel and K. Joulain, Europhys. Lett. **72**, 929–935 (2005).
[379] J. Ma, Q. Zhao, and Y. Meng, Phys. Rev. B **89**, 075421 (2014).
[380] M. G. Silveirinha and S. I. Maslovski, Phys. Rev. Lett. **105**, 189301 (2010).
[381] A. Lambrecht, M. T. Jaekel, and S. Reynaud, Phys. Lett. A **225**, 188–194 (1997).
[382] G. L. Klimchitskaya, B. Geyer, and V. M. Mostepanenko, International Journal of Modern Physics A **25**(11), 2293–2301 (2010).
[383] L. Duraffourg and P. Andreucci, Phys. Lett. A **359**, 406–411 (2006).
[384] A. Lambrecht, I. Pirozhenko, L. Duraffourg, and P. Andreucci, Europhys. Lett. **77**(4), 44006 (2007).
[385] F. Chen, G. L. Klimchitskaya, V. M. Mostepanenko, and U. Mohideen, Phys. Rev. Lett. **97**(17), 170402 (2006).
[386] R. Esquivel-Sirvent, J. Appl. Phys. **102**, 034307 (2007).
[387] O. Kenneth and I. Klich, Phys. Rev. Lett. **97**, 160401 (2006).
[388] S. J. Rahi, M. Kardar, and T. Emig, Phys. Rev. Lett. **105**, 070404 (2010).
[389] G. Palasantzas, J. V. Zwol, and J. T. M. d. Hosson, Appl. Phys. Lett. **93**, 121912 (2008).
[390] M. Lisanti, D. Iannuzzi, and F. Capasso, Proc. Nat. Ac. Sci. USA **102**, 11989–11992 (2005).
[391] D. Iannuzzi, M. Lisanti, J. N. Munday, and F. Capasso, J. Phys. A: Math. Gen. **39**, 6445–6454 (2006).
[392] G. Gómez-Santos, Phys. Rev. B **80**, 245424 (2009).
[393] A. P. McCauley, A. W. Rodriguez, M. T. H. Reid, and S. G. Johnson, arXiv 1105.0404 (2011).
[394] K. A. Milton, E. K. Abalo, P. Parashar, and N. Pourtolami, Phys. Rev. A **83**, 062507 (2011).
[395] V. A. Parsegian and G. H. Weiss, J. Adh. **3**(4), 259–267 (1972).
[396] Y. Barash, Izv. Vyssh. Uchebn. Zaved. Radiofiz. [Radiophysics and Quantum Electronics 12] **12**, 1138 (1978).
[397] S. J. van Enk, Phys. Rev. A **52**(4), 2569–2575 (1995).
[398] J. N. Munday, D. Iannuzzi, Y. Barash, and F. Capasso, Phys. Rev. A **71**, 042102 (2005).
[399] M. B. Romanowsky and F. Capasso, Phys. Rev. A **78**, 042110 (2008).
[400] H. Razmi and S. M. Modarresi, Int. J. Theor. Phys. **44**(2), 229–234 (2005).
[401] O. Kenneth and S. Nussinov, arXiv:hep-th/0001045 (2000).
[402] R. B. Rodrigues, P. A. Maia Neto, A. Lambrecht, and S. Reynaud, Europhys. Lett. **75**(5), 822–828 (2006).
[403] F. M. Serry, D. Walliser, and M. G. Jordan, J. Microelec. Sys. **4**(4), 193–205 (1995).
[404] A. Ashourvan, M. Miri, and R. Golestanian, Phys. Rev. Lett. **98**(14), 140801 (2007).
[405] M. Imboden, J. Morrison, D. K. Campbell, and D. J. Bishop, arXiv 1404.3315 (2014).
[406] M. P. Bendsoe and O. Sigmund, Topology Optimization, 2nd edition (Springer, 2003).